Decoding natural astrocyte rhythms: dynamic actin waves result from environmental sensing by primary rodent astrocytes

Kate M. O'Neill[1]†, Emanuela Saracino[2]†, Barbara Barile[3], Nicholas J. Mennona[1,4], Maria Grazia Mola[3], Spandan Pathak[1], Tamara Posati[2], Roberto Zamboni[2], Grazia P. Nicchia[3], Valentina Benfenati[2*], Wolfgang Losert[1,4*]

[1] Inst. for Physical Science and Technology, Univ. of Maryland, College Park, MD, USA
[2] Inst. of Organic Synthesis and Photoreactivity, National Research Council of Italy, Bologna, Italy
[3] Dept. of Biosciences, Biotechnology and Biopharmaceutics, Univ. of Bari Aldo Moro, Bari, Italy
[4] Physics Dept., Univ. of Maryland, College Park, MD, USA

† equal contributions as co-first authors
** valentina.benfenati@isof.cnr.it and wlosert@umd.edu (equal contributions as co-corresponding authors)*

Abstract

Astrocytes are key regulators of brain homeostasis, an important physiological process that includes but is not limited to buffering of extracellular K^+, equilibrating osmotic gradients, regulating pH, uptake of neurotransmitters, and releasing growth factors – all of which are essential for proper cognitive function. While previous studies have revealed how specific molecular components of the astrocytic cytoskeleton affect the efficacy of these homeostatic processes, none have studied how homeostasis is linked to the excitable systems character of the cytoskeleton. As recently discovered, excitability of the actin cytoskeleton manifests in second-scale dynamic fluctuations and acts as a sensor of chemo-physical environmental cues. Here we find that homeostatic regulation may be more active than previously thought, involving the excitable dynamics of actin in certain subcellular regions, especially near the cell boundary. Our results further indicate that actin dynamics concentrates into "hotspot" regions that selectively respond to certain chemo-physical stimuli, specifically the homeostatic challenges of ion or water concentration increases. Substrate topography makes the actin dynamics of astrocytes weaker. Superresolution images demonstrate that surface topography is also associated with predominant perpendicular alignment of actin filaments near the cell boundary whereas flat substrates result in an actin cortex mainly parallel to the cell boundary. Additionally, co-culture with neurons increases both the probability of actin dynamics and the strength of hotspots. The excitable systems character of actin thus makes astrocytes direct participants in neural cell network dynamics.

Keywords: astrocytes, actin, cytoskeleton, dynamics, co-culture

Abbreviations: stimulated emission depletion (STED); cytoskeletal excitable network (CEN); signal transduction excitable network (STEN); poly-D-lysine hydrobromide (PDL); hydrotalcite-like compound (HTlc); glial fibrillary acidic protein (GFAP); phosphate buffered saline (PBS); regions of interest (ROIs); Laplacian of Gaussian (LoG); analysis of variance (ANOVA)

ORCiD

Kate M. O'Neill	0000-0003-4397-5767
Nicholas J. Mennona	0000-0001-8595-0336
Maria Grazia Mola	0000-0002-4421-9237
Spandan Pathak	0000-0001-7866-2096
Tamara Posati	0000-0002-3879-266X
Roberto Zamboni	0000-0003-3739-2207
Grazia P. Nicchia	0000-0002-4257-514X
Valentina Benfenati	0000-0002-2858-8497
Wolfgang Losert	0000-0002-1792-7860

Author contributions

Conceptualization: VB WL
Surface preparation: ES TP
Experiments: KMO ES BB MGM
Analysis: KMO NJM SP
Interpretation: KMO ES BB NJM MGM GPN VB WL
Supervision: GPN VB WL
Writing—original draft: KMO ES BB NJM GPN VB WL
Writing—review & editing: KMO ES BB NJM MGM SP TP RZ GPN VB WL

Statements and Declarations:

Conflict of interest: The authors have no competing interests to declare.

Ethics approval: This research required isolating primary astrocytes from neonatal rats, and all animals' care was in accordance with institutional guidelines at the authors' respective universities: the Institutional Animal Care and Use Committee at the University of Maryland (protocols R-JAN-18-05 and R-FEB-21-04) and the Italian Ministry of Health for the University of Bologna (ethical protocol number ID 360/2017 PR).

Consent for publication: All authors consent to the publication of this manuscript.

Data and materials availability: All data and code will be made available in a repository located in the Losert laboratory's github page.

Acknowledgements and Funding:

The authors would like to thank the University of Maryland Imaging Incubator Core Facility for providing and maintaining the systems used in collecting images for this work. They also thank Q. Yang and L. J. Campanello for helpful discussions related to analysis.

This work was supported by the following grants:

US Air Force Office of Scientific Research MURI grant FA9550-16-1-0052 to WL

US Air Force Office of Scientific Research grant FA9550-19-1-0370 (AstroDyn) to WL VB GPN KMO

US Air Force Office of Scientific Research FA9550-20-1-0386 to (ASTROLIGHT) to VB

US Air Force Office of Scientific Research FA9550-20-1-0324 to GPN

HORIZON EUROPE SEEDS INTERGLIO (S08) funded by the University of Bari Aldo Moro to GPN

NIH R21NS116892-01 to GPN
US Air Force Office of Scientific Research FA9550-18-1-0255 (3D Neuroglia) to VB
COMBINE fellowship to NJM

Introduction

The ability of the brain to receive and compute information depends on the unique abilities of its component brain cells. After each neuronal action potential, the concentrations of ions and water are altered in the perineural and perivascular spaces. Specifically, the concentration of potassium in these areas may be as high as 60-100 mM [1-3] in pathophysiological situations. One of astrocytes' homeostatic functions is to balance extracellular potassium concentration through potassium uptake and spatial buffering [4-12]. This process relies on the sodium/potassium pump (Na^+/K^+ ATPase), potassium channels from the inward rectifier superfamily, and gap junctional coupling. Moreover, this transmembrane flux of K^+ is also accompanied by osmotically-driven water movement and intracellular calcium signaling [13-16].

With a stellate morphology [17-19], astrocytic processes contact neurons and blood vessels and therefore play critical roles in coupling the neuronal with the vascular activities of the brain [20]. Perisynaptic astrocytic processes (PAPs) and perivascular astrocytic processes (PvAPs) represent functional microdomains and are enriched with water and ion channels that allow astrocytes to precisely control the extracellular environment through continuous sensing and balancing of local ionic changes (between neurons for PAPs and at the blood vessel interface for PvAPs) in response to neuronal network activity [21-23,20,24-26]. At the same time, the gap junctional coupling between astrocytes serves as a signaling mechanism enabling synchronicity and lateral communication between astrocytes within the larger astroglia syncytia [27,28].

Though astrocytic communication via gap junctional coupling enables dynamic exchange between cells at the ionic and molecular scales [1,27,29,28], questions remain how these small scale dynamics couple with, modulate, and impact responses at larger length scales, such as within astroglial cell networks or the whole brain. In particular, gap junctions participate in potassium spatial buffering by aiding in the dispersion of excess K^+ through the astroglial syncytium [5,4,6,7,1] and are also implicated in the propagation of astrocytic calcium waves, a form of extraneuronal signaling [30-34]. The efficiency of these homeostatic processes [35,36] is considered the basis for astrocytes' involvement in cognitive functions while their impairment may cause pathologies ranging from edema to epilepsy [16].

More recently, the importance of astrocytes' structural and functional properties has been highlighted for organ- and system-level functions, including synaptic plasticity, memory formation, learning, and regulation of sleep and metabolic activity [37,38]. Here we investigate the actin cytoskeleton as an integrator from the molecular to the systems scale due to its ability to self-assemble into dynamic networks. Indeed, experiments on fixed cells have revealed the key molecular players regulating changes to astrocyte morphology, including but not limited to Rac1 and RhoA GTPases [39-44] and the Arp2/3 complex [45], all of which play a role in promoting, maintaining, or reversing the stellate morphology typical of differentiated astrocytes [46]. Other recent studies on fixed cells have also indicated that the astrocytic actin cytoskeleton plays a role in several homeostatic processes, such as volume regulation and potassium spatial buffering [47-49].

However, much less is known about the second-scale dynamics of the actin cytoskeleton in these cellular processes. For migrating cells – such as neutrophils, metastatic cancer cells, and even

microglia – actin dynamics had been mostly considered as a facilitator of changes in cell morphology. For example, a recent study in T cells demonstrated the importance of global (whole cell) actin dynamics in facilitating immunological synapse formation [50]. New lines of research, though, are also investigating the importance of actin dynamics in crucial cell processes. Dynamic actin has been shown to be important for biological function [51,52], such as surveillance of the brain parenchyma by microglia [53]. Notably, actin cytoskeletal dynamics are necessary for relaying biomechanical forces at the synapse [54], indicating that mechanical signals (in addition to the well-studied chemical and electrical signals) are critical for synaptic transmission and, therefore, cognitive function.

Moreover, recent studies across multiple cell types have demonstrated that the actin cytoskeleton is not only dynamic when a cell changes shape and moves but is also an excitable system with its own intrinsic dynamics, including sustained waves and oscillations that persist independently of changes to cell shape [55-64]. The source of actin dynamics is thought to be twofold: i) a cytoskeletal excitable network of proteins (CEN) that drives cycles of polymerization and depolymerization typically lasting a few seconds, and ii) a signal transduction excitable network (STEN) that can self-organize these local oscillations into larger scale waves that drive cell migration [51,59,65,58]. We propose that, in astrocytes, CEN dynamics dominate, thus leading to local actin dynamics that is stationary in space and occurs on a second timescale. Therefore, CEN could carry information about homeostatic challenges that occur at the nanometer, ionic, and molecular scales.

Here we study how the actin cytoskeleton serves as the bridge from these smaller scales (e.g., ions) to larger scales (e.g., cells) and facilitates the global (cellular level) homeostatic response of astrocytes. We analyze actin dynamics using optical flow [60,66] and perform shape analysis [67,57,68] on timelapse images of live primary astrocytes transduced with actin-GFP. We demonstrate that actin dynamics occurs in astrocytes and that it can be triggered by extracellular environment modifications, such as an increase in ion concentrations or a change in culturing environment. The spatial distribution of the actin dynamics is localized near the boundary of the cell and is concentrated into active clusters we term “hotspots”.

Notably, the strength of actin dynamics changes depending on whether the exposure is to an increase in extracellular potassium or to hypotonic challenge, abbreviated as “high K^+” and “hypotonic”, respectively. We refer to the application of these solutions to cultures as “triggering” conditions because they have been shown to mimic pathophysiological changes in the extracellular milieu similar to epilepsy [69] or edema [70] and to cause responses in astrocytes that range from swelling to calcium waves [71,72,3,73-77,48,78]. In addition, activity identified in the processes of differentiated astrocytes, induced by nanotopography [79], is weaker when compared to polygonal astrocytes, which have the shape characteristic of undifferentiated astrocytes grown in the absence of neurons [80-84]. Surprisingly, astrocytes co-cultured with neurons show more frequent dynamics than polygonal cells, and the dynamics were of comparison magnitude. Finally, superresolution imaging by STimulated Emission Depletion (STED) microscopy and analysis with a filament extraction algorithm demonstrates that the specific orientation of actin filament structures occurs only in differentiated cells, indicating that both structure and dynamics carry information about the environment. Overall, our results indicate that actin is dynamic in astrocytes and behaves collectively by clustering into

"hotspot" regions that respond in distinct ways to specific chemo-physical stimuli and may drive the homeostatic response of the neural cell network.

Materials and Methods

Rat cortical astrocyte culture preparation, maintenance, plating, and differentiation

Cell culture:

Primary astrocytes were obtained from Sprague Dawley rats housed at the University of Maryland (in concordance with the recommendations of and approval by the University of Maryland Institutional Animal Care and Use Committee; protocols R-JAN-18-05 and R-FEB-21-04) or from Wistar rats housed at the University of Bologna (in concordance with the Italian and European law of protection of laboratory animals and the approval of the local bioethical committee, under the supervision of the veterinary commission for animal care and comfort of the University of Bologna and approved protocol from Italian Ministry of Health; ethical protocol number ID 360/2017 PR, released on May 2017, valid for 5 years).

Primary cultures of astrocytes were prepared as described by McCarthy and de Vellis [85] from newborn rat pups between postnatal days 1 and 2 [14,86,87]. Briefly, neonatal cerebral cortices devoid of meninges were gently triturated, filtered with a 70 µm cell strainer (**cat. no. 22-363-548**; Fisher Scientific, MA, USA), and plated in T25 cell culture flasks (**cat. no. 229331**; CELLTREAT Scientific Products, MA, USA) containing Dulbecco's Modified Eagle Medium with GlutaMAX and high glucose (DMEM; **cat. no. 10-566-024**; Fisher Scientific, MA, USA) supplemented with 15% fetal bovine serum (FBS; **cat. no. 100-106**; Gemini Bio-Products, CA, USA) and penicillin-streptomycin (P/S) at 100 U/mL and 100 µg/mL, respectively (P/S; **cat. no. 15070063**; Thermo Fisher Scientific, MA, USA). Flasks were maintained in an incubator at 37 °C, 5% CO_2, and proper humidity levels for two weeks. During this period, we replaced cell medium every two days, and flasks were gently shaken when necessary to remove undesired microglial cells. When confluence was reached, astrocytes were dispersed using trypsin-EDTA 0.25% (**cat. no. 25200056**, Thermo Fisher Scientific, MA, USA), and the cell suspension was re-plated on coverslips or in imaging dishes functionalized with Poly-D-lysine hydrobromide (PDL; **cat. no. P7886**; Sigma-Aldrich, MO, USA) as previously described [79,88-90,86] or with HTlc as previously described [91,79]. Cells were plated at a density of $5\text{-}10\times10^3$ per imaging dish and maintained in DMEM containing 10% FBS and 1% P/S.

For co-culture experiments, astrocytes were prepared as described above. At one to two weeks after the astrocyte dissection, neurons were prepared as previously described from rats at embryonic day of gestation 18 (E18) [92-97]. Briefly, embryos were removed via Caesarian section and decapitated. Cerebral hemispheres were separated, and meninges were removed. The hippocampi and cortices were dissected, and cortices were combined and manually triturated. Cortical neurons were plated in imaging dishes coated with PDL at a density of 5×10^5 cells/dish and were maintained in NbActiv4 medium (**cat. no. Nb4-500**, BrainBits, TN, USA) with 1% P/S. When astrocyte flasks reached confluence, astrocytes were added to the neuronal culture at a density of $1\text{-}2\times10^5$ cells/dish, and the media was changed to DMEM with 10% FBS and 1% P/S.

As can be seen in **Suppl. Fig. 1**, plating density was chosen to ensure that cultures were not confluent (which would prevent reliable transduction) and also that astrocytes were not isolated (which could affect dynamics).

PDL and HTlc film preparation:

Plastic dishes with glass inserts (**cat. no. P35G-1.0-20-C**, MatTek, MA, USA) or glass coverslips were functionalized with PDL to serve as a control surface or with Zn-Al hydrotalcite nanoparticles (HTlc) to induce morphological differentiation of astrocytes. For live imaging, PDL was used at a working concentration of 0.1 mg/mL. For STED imaging, PDL was used at a working concentration of 0.01 mg/mL. In both cases, coverslips were coated with PDL for 20 minutes at room temperature and washed three times with approximately 500 µL of sterile H_2O. Coverslips or dishes were functionalized with HTlc by adding the HTlc suspension drop by drop on the coverslips and allowed to dry overnight. Once dried, the HTlc coverslips were sterilized by UV for approximately 30 min. For live imaging, astrocytes grown on PDL and HTlc were cultured for three to seven days after replating prior to imaging, and co-cultured astrocytes were cultured for two to three days prior to imaging. For co-culture imaging, neurons were between 4 and 18 days *in vitro*. For STED imaging, astrocytes were cultured for five days after replating prior to fixation.

Transduction of cells with actin-GFP

To visualize actin dynamics, we chose to transduce astrocytes with CellLight Actin-GFP, BacMam 2.0 (**cat. no. C10506**; ThermoFisher Scientific, MA, USA) because it has minimal toxicity and sparsely labels cells, which is ideal for single cell analysis. For PDL and HTlc cells, transduction occurred in the imaging dish at a concentration of 100 particles per cell (PPC). At 48 hr prior to live imaging, 5-10 µL (depending on the plating density) of the reagent was added to the cell culture media. A full media change was performed 16-20 hr after transduction, and imaging was performed 24-48 hr after the full media change. For co-cultured astrocytes, transduction occurred in the flask at a concentration of 10 PPC. At 24 hr prior to plating, 100 µL of the reagent was added to the cell culture medium within the flask. Plating was performed 16-20 hr after transduction. Imaging was performed 48-72 hr after plating.

Live confocal imaging of transduced astrocytes

Live imaging timelapses were acquired at the University of Maryland CMNS Imaging Core using a PerkinElmer spinning disk confocal microscope with an oil immersion 40x objective (1.30 NA; 0.36 µm/pixel) and under temperature, CO_2, and humidity control. The microscope was equipped with a Hamamatsu ImagEM X2 EM-CCD camera (C9100-23B), which recorded 16 bit images. Data acquisition was performed with PerkinElmer's Volocity software (version 6.4.0). A subset of timelapses were taken at the CNR on an inverted confocal microscope (Crisel Instruments) using a 40x water immersion objective (0.16 µm/pixel).

Transduced astrocytes were identified by a positive signal in the 488 nm laser channel. After imaging parameters were set, the media was changed from growth media to standard external solution (control) followed by one of the triggering conditions (high potassium solution or hypotonic solution). Single-plane images were acquired every 2 sec in the 488 channel. A consistent z-plane was assured with Perfect Focus (Nikon PFS).

280
281 Immunostaining and superresolution imaging of fixed astrocytes
282
283 *Antibodies:*
284 Mouse monoclonal Anti-Glial Fibrillary Acidic Protein (GFAP) antibody (diluted 1:200;
285 **cat. no. G3893**; Sigma-Aldrich, MO, USA) and Goat anti-Mouse IgG (H+L) Highly Cross-
286 Adsorbed Secondary Antibody, Alexa Fluor 594 (diluted 1:300; **cat. no. A-11032**; Thermo
287 Fisher Scientific, MA, USA) were used as primary and secondary antibody, respectively, for
288 GFAP immunostaining. Alexa Fluor 488 Phalloidin (diluted 1:500; **cat. no. A12379**; Thermo
289 Fisher Scientific, MA, USA) was used for direct labelling of actin.
290
291 *STED immunostaining:*
292 Immunofluorescence for gated STED (gSTED) was performed as indicated in the Quick Guide
293 to the STED Sample Preparation (www.leica-microsystems.com), with some slight adjustments
294 as previously reported [98,99]. Astrocytes were plated on the PDL and HTlc-treated coverslips
295 and cultured for five days. On the fifth day of culture, cells were fixed with 2%
296 paraformaldehyde (**cat. no. P6148**; Sigma-Aldrich, MO, USA) in phosphate buffered saline
297 (PBS) for 10 min, washed with PBS, and permeabilized with 0.3% Triton X-100
298 (**cat. no. T8787**; Sigma-Aldrich, MO, USA) for 10 min. After blocking with 0.1% gelatin in
299 PBS, fixed astrocytes were incubated with GFAP-primary antibody for 1 hr at room temperature.
300 Cells were then rinsed with 0.1% gelatin-PBS and co-incubated with Alexa Fluor 488 Phalloidin
301 and Alexa Fluor 594-conjugated secondary antibody for 1 hr at room temperature. After washing
302 with PBS, coverslips were mounted on microscope slides by using the ProLong Glass Antifade
303 Mountant (**cat. no. P36980**; Thermo Fisher Scientific, MA, USA) without DAPI, as indicated in
304 Leica official guide, and imaged with both confocal and STED microscopy.
305
306 *STED imaging:*
307 Confocal and STED images of fixed astrocytes grown on PDL and HTlc were acquired using a
308 Leica TCS SP8 3X microscope, provided with AOTF and AOBS, white light laser (WLL),
309 Hybrid Detectors (HyD), and two STED lasers (592 nm, 660 nm) [99]. A Leica HC PL APO
310 100x/1.40 NA Oil STED White objective and Type F Immersion liquid with a refractive index of
311 1.5 were used. Before starting imaging, the excitation and the doughnut-shaped STED beams
312 were switched on (WLL set laser power= 70%; STED-592 nm set laser power = 98%), aligned,
313 and allowed to reach operating temperature. The beam alignment was repeated whenever
314 necessary. Excitation of the Alexa Fluor 488 dye was achieved using a continuous-wave 488 nm
315 laser line (NKT Photonics supercontinuum laser). For superresolution imaging of actin, g-STED
316 was performed using the continuous wave 592 nm-emitting STED fiber laser. More detailed
317 acquisition settings are reported in **Table 1**. All confocal and STED images were acquired at a
318 set room temperature of 20 °C under constant Acquisition Mode settings (Format scanning
319 resolution: 1024x1024 pixels; Scan Speed: 100 Hz).
320
321 *Criteria for acquisitions of ROIs:*
322 Single or few and well-spaced cells were preferentially chosen for STED imaging to ensure no
323 overlap of actin structure belonging to different cells. Actin and GFAP images of the whole cell
324 were first acquired by confocal microscopy at an original magnification of 100x. Then, multiple
325 random regions of interest (ROIs) (~20x20 µm sized) were selected and imaged using an extra

326 optical zoom (from 5 to 7) by confocal and STED microscopy. Three independent experiments
327 were conducted.
328
329 Synthesis of ZnAl-HTlc nanoparticles and film preparation
330 Colloidal aqueous dispersion of ZnAl-HTlc nanoparticles having the formula
331 $[Zn_{0.72}Al_{0.28}(OH)_2]\ Br_{0.28}\ 0.69\ H_2O$ were prepared by the double-microemulsion technique
332 previously described [79]. For the film preparation, a 125 or 160 µL aliquot of ZnAl-HTlc
333 colloidal dispersion at a concentration of 1.2 mg/mL was dropped onto 15 or 19 mm diameter
334 glass coverslips and successively dried for 4 hr in a sterile hood. The obtained ZnAl-HTlc films
335 were used to culture astrocytes and as substrates for live dynamics imaging and fixed STED
336 imaging as described above. In this manuscript, the ZnAl-HTlc films are referred to simply as
337 HTlc.
338
339 Solutions and chemicals
340 All salts and chemicals employed for the investigations were of the highest purity grade. For live
341 imaging experiments, the standard external solution ("control") was the following (mM):
342 140 NaCl, 4 KCl, 2 $MgCl_2$, 2 $CaCl_2$, 10 HEPES, 5 glucose, pH 7.4 with NaOH and osmolarity
343 adjusted to ~315 mOsm with mannitol. When using external solutions with different ionic
344 compositions, such as the high potassium solution ("high K^+", [40 Mm]), salts were replaced
345 equimolarly. The hypotonic extracellular solution ("hypotonic") of 260 mOsm/L was obtained
346 by omitting mannitol in the control solution. When imaging, media was changed carefully to
347 prevent accidental, mechanical stimulation of cells with the pipette. Moreover, we controlled for
348 any effects that changing media might cause by changing media prior to imaging under control
349 conditions (from growth media to the standard external solution) and under triggering conditions
350 (from the standard external solution to high K^+ or hypotonic medium).
351
352 Analysis of live imaging data
353
354 *Pre-processing of timelapses:*
355 All timelapses were smoothed in time using a Simoncelli smoothing filter [100]. Prior to
356 smoothing, any timelapses that showed noticeable jitter or drift due to thermal gradients were
357 processed through a jitter correction algorithm using discrete Fourier transform (DFT)
358 registration and an upsampling factor of 100 (using the "dftregistration" code package from
359 [101]). For timelapses where drift was inconsistent and unable to be fully corrected with the DFT
360 method, an additional correction using intensity-based image registration (via the MATLAB
361 functions "imregconfig" and "imregister") was applied using the average image of the DFT
362 corrected timelapse as the fixed image.
363
364 *Shape analysis and identification of bulk and boundary regions:*
365 We used shape analysis to identify cell boundaries and subsequently to be able to compare actin
366 dynamics within different regions of astrocytes. Using a snake algorithm from our previous
367 work [67,57,68], we analyzed the average fluorescent image of each cell to generate the "true
368 boundary" (**see Fig. 1A-B**). Prior to shape analysis, images were smoothed ("imgaussfilt" in
369 MATLAB with a standard deviation of 1.0) and subsequently sharpened ("imsharpen" in
370 MATLAB with a radius of 2.5 and amount of 1.0). Alpha and beta parameters for the snake
371 algorithm (tension and rigidity, respectively) were 0.20 and 0.25, respectively. We found that

this true boundary tended to capture the most prominent morphological features of the cell but often excluded regions that were only transiently dynamic. To mitigate this challenge, we eroded or dilated the true boundary using a spherical structural element with a radius of 10 pixels. By subtracting the eroded cell region from the dilated cell region, we identified a boundary region. We considered the eroded cell mask to be the bulk region.

Optical flow analysis of actin dynamics:

Optical flow analysis similar to that used in [60] was performed on smoothed and jitter-corrected timelapses in Python 3.8. The optical flow weight matrix was a 19x19 pixel Gaussian with a standard deviation of 3 pixels (1.1 μm) for all timelapses taken at UMD. For a small subset of HTlc timelapses taken at the CNR, the optical flow weight matrix was a 41x41 pixel Gaussian with a standard deviation of 6.75 pixels (1.1 μm). The truncation value for the Gaussian kernel was consistently set to 3. Because actin dynamics in astrocytes is less prominent than in migrating cells usually studied by our lab [60,56], we only considered optical flow vectors with the highest 1% of magnitude within the dilated cell boundary that also passed our reliability criteria (at least 33% of the mean reliability value for that timelapse). These strict criteria ensured that we were only considering dynamic actin events that are large and reliable compared to background noise.

Segmentation of active regions ("hotspots") of actin dynamics:

To identify regions with the most actin activity, we further analyzed our thresholded data by eroding and dilating in the x, y, and time dimensions using an elongated cube with dimensions of [3,3,2]. To ensure that we were not including regions of low activity, we set an event probability threshold of 0.10, meaning that a region had to be active at least 10% of the time to be considered a "hotspot". Furthermore, we imposed a size constraint of 20 pixels (including the time dimension) to ensure that any active regions did not just barely meet the volume require of 3x3x2. Since the dynamics within HTlc cells are on a smaller scale, the hotspot analysis did not reveal any regions that were clearly active.

Analysis of STED images of fixed astrocytes

Laplacian of Gaussian (LoG) filtering to segment actin:

To characterize the organization of the actin meshwork in STED images of fixed cells, as shown in **Fig. 5**, we performed several image processing techniques using custom-written algorithms in MATLAB (Mathworks). Prior to processing, all STED images are adjusted using a contrast-limited adaptive histogram equalization ("adjusthisteq" function in MATLAB's proprietary API (https://www.mathworks.com/help/images/adaptive-histogram-equalization.html). The resolution of the STED images is 16.18pix/nm. Next, each image is convolved with an anisotropic, rotating Laplacian of Gaussian (LoG) kernel. The exact kernel parameters were determined through trial and error to approximately match the cylindrical shape of actin as visualized by Phalloidin-488 staining. The number of angles through which the LoG kernel is rotated was chosen to balance computational time and segmentation accuracy. For each pixel, the best match angle is chosen via the maximum value resulting from convolving that pixel with all rotations of the filter, and a threshold is applied to ensure a high-quality match. This processing results in a filtered image that highlights both the actin organization and the angle associated with each filament extracted from kernel (see **Fig. 5A1**). The angles associated with the extracted actin are defined in terms of

the Cartesian coordinate system, which is not biologically meaningful. To establish the angle at which the actin organizes relative to the cellular boundary, we manually draw a boundary for each cell. The number of pixels per boundary varies on a cell-to-cell basis. For each pixel, we derive the angle of that pixel's actin relative to the closest boundary point. This transformation generates angles in the range of 0 to $\pi/2$. We then apply an additional threshold at an arbitrary value to only segment the longest actin (**Fig. 5A2**); doing so greatly reduces the noise in our processed data. We analyzed at least 15 individual cells per nanotopographic surface, and the morphologies of the imaged areas varied from cell to cell. Thus, the boundaries are generated to normalize the distributions of the relative angles across the data sets. We noticed that for the STED images taken of astrocytes grown on HTlc, there is more total boundary per unit-area. Thus, the boundaries from which the relative angles are calculated are drawn to coincide with only the leading edge of the cell (see **Fig. 5B** for representative examples).

Cluster analysis of relative angles:

To understand how astrocytic actin organization differs when the cells are grown on different nanotopographies, we use a hierarchical cluster analysis from MATLAB's proprietary API (https://www.mathworks.com/help/stats/cluster-analysis.html). From the relative angle distributions across both PDL and HTlc (22 individual cells and 15 individual cells, respectively), we group the distributions into "parallel" (angles between 0 and $\pi/6$) and "perpendicular" (angles between $\pi/3$ and $\pi/2$), as shown in **Fig. 5B**. As inputs to the clustering algorithm, we use the fractions of "parallel" and "perpendicular" actin of the 37 individual cells but do not include information about the corresponding nanotopographic surface. We then use the "pdist," "linkage," "cophenet," and "linkage" functions (while optimizing the cophenetic coefficient of our 'distance' and 'linkage' parameters) to generate predictive clusters of the input data.

Data representation and statistics

All data were plotted and all statistical tests performed in MATLAB 2021a. For data showing differences between control and triggering or between boundary and bulk regions, paired t-tests were used ("ttest" function in MATLAB). For data in **Fig. 3** comparing PDL to HTlc to Co, one-way analysis of variance (ANOVA) tests were used ("anova1" function). For data in **Fig. 4** comparing PDL to CO, unpaired two-sample t-tests were used ("ttest2" function). When analyzing probability of actin dynamics vs. distance, ANOVA tests were used as follows: repeated measures ANOVA for paired data in **Fig. 1** ("fitrm" and "ranova" functions), and two-way ANOVA to compare PDL to HTlc to Co in **Fig. 3** ("anovan" function). For all ANOVA tests, Tukey's multiple comparisons test ("multcompare" function) was used as the post test. All errorbars indicate 95% confidence interval, and the significance level was set at $\alpha=0.05$. Adobe Illustrator (version 25.0.1) was used for final assembly of all figures.

Results

Primary astrocytes display actin dynamics in response to chemical cues

Our live imaging results demonstrate that astrocytes consistently display actin dynamics, particularly near the boundary of the cell. Representative overlays of fluorescent images are

shown in **Fig. 1A** (A1 and inset for representative control timelapse; A2 and inset for representative "triggering" timelapse). In this representation, a perfectly stationary cell would appear all white; the presence of different colors indicates non-overlapping structures at either earlier (more blue) or later (more red) times. To quantify actin dynamics, we employ an optical flow method [102] similar to that used in our previous work [60]. We additionally use shape analysis [67,57,68] to separately consider actin dynamics within the whole cell, boundary region, and bulk region (see **Fig. 1A3-4** for representative analyses and **Fig. 1B** for schematic and *Materials and Methods* for more detail).

To obtain an overall picture of how actin dynamics changes between control and triggering conditions, we first quantified the strength of actin dynamics within specific subcellular regions, specifically the boundary region and bulk region (**Fig. 1C1**). Only triggering with hypotonic causes an increase in the strength of actin dynamics within the boundary region ($p=0.040$ for control vs. hypotonic via paired t-test). We do not observe significant differences in actin dynamics strength within the boundary after triggering with high K^+ ($p=0.147$ for control vs. high K^+ via paired t-test) or within the bulk for either triggering condition ($p=0.696$ and $p=0.052$ for control vs. high K^+ and for control vs. hypotonic, respectively, via paired t-test). Notably, neither of the triggering conditions changes the probability of actin dynamics within the boundary or bulk regions (**Suppl. Fig. 2A1**).

We next wanted to understand whether actin dynamics becomes more probable within the boundary region after a triggering stimulus. To accomplish this, we calculate the fraction of dynamics within the boundary and find a significant shift in actin dynamics towards the boundary after triggering with hypotonic but not after triggering with high K^+ (**Fig. 1C2**; $p=0.881$ and $p=0.013$ for control vs. high K^+ and for control vs. hypotonic, respectively, as determined by paired t-test).

To delve into distance dependence of actin dynamics more closely, we quantify the distance from instances of actin dynamics to the cell boundary (true boundary shown in **Fig. 1B**). Curves of the representative cells shown in **Fig. 1A** are shown in **Fig. 1D1** with the boundary and bulk regions labeled. Since we are most interested in the high actin activity near the boundary, we compare how the probability of actin dynamics changes over distance when comparing the two triggering conditions to their matched controls. High K^+ cells display no difference in actin dynamics at specific distances within the boundary region (**Fig. 1D2**). In contrast, hypotonic cells are significantly more likely to show actin dynamics within the boundary region compared to matched controls, specifically between 1.44 and 2.52 μm from the boundary ($p<0.05$ for control vs. hypotonic all distances in that range as determined by repeated measures ANOVA; refer to **Fig. 1D3** legend for exact p-values). Taken together with the data from **Fig. 1C2**, we show that a higher probability of actin dynamics at specific distances after hypotonic challenge is indeed accompanied by an overall shift to the boundary region.

These results indicate the following: i) actin dynamics has a higher probability of occurring under hypotonic conditions (**Fig. 1C1**); ii) increased probability of actin dynamics at specific distances is observed when cells are exposed to hypotonic challenge (**Fig. 1D3**); and iii) this increase at specific distances after hypotonic challenge is also reflected in the overall probability

of actin dynamics (**Suppl. Fig. 2A1**) and in the shift of actin dynamics to the boundary (**Fig. 1C2**).

Finally, we also used inhibitors of the inwardly rectifying K^+ channel Kir4.1 (barium [Ba^{2+}]) and of gap junctions (carbenoxolone [CBX]), involved respectively in potassium spatial buffering [103,104] and cell volume regulation in astrocytes [105,106], to provide a more mechanistic view of how chemical triggering with high K^+ and hypotonic media changes actin dynamics. These inhibitors decrease actin dynamics such that robust analysis was not possible (representative fluorescent overlays and analysis provided in **Suppl. Fig. 3**). Future studies will attempt to study the effects of these inhibitors when actin dynamics are in a more excited state.

<u>Actin dynamics within astrocytes is clustered into active "hotspot" regions</u>

While characterizing actin dynamics within astrocytes, we noticed that many cells seemed to have active regions near the boundary (**Fig. 2A1**) that we suspected were responsible for most of the actin dynamics. To identify these "hotspot" regions, we apply the image processing techniques of erosion and dilation to identify areas of persistent activity (**Fig. 2A2**). After applying thresholds for activity magnitude and probability and hotspot size, we segment regions that meet these criteria (**Fig. 2A3** and inset).

We first compared the strength of actin dynamics within the hotspot regions, considering the boundary and bulk regions separately as before. In contrast to what we found in **Fig. 1C1** (stronger actin dynamics in the boundary region after hypotonic challenge), we find within hotspot regions that actin dynamics is stronger only in cells exposed to high K^+ and only within the boundary region (**Fig. 2B1**; boundary: $p=0.006$ for control vs. high K^+ and $p=0.435$ for control vs. hypotonic as determined by paired t-test; bulk: $p=0.339$ for control vs. high K^+ and $p=0.298$ for control vs. hypotonic as determined by paired t-test).

We also investigated the relative strength of hotspot dynamics where the average magnitude within hotspots is normalized by the average magnitude of dynamics within the whole cell (**Fig. 2B2**). When comparing this relative strength between cells in triggering conditions and their matched controls, we find that only high K^+ cells display significantly stronger actin dynamics within hotspot regions compared to the whole cell ($p=0.006$ for control vs. high K^+ and $p=0.639$ for control vs. hypotonic as determined by paired t-test). Finally, we investigated whether actin dynamics in these hotspot regions is more persistent and find that the duration is not significantly different for either high K^+ cells or hypotonic cells compared to matched controls (**Fig. 2B3**; $p=0.056$ for control vs. high K^+ and $p=0.491$ for control vs. hypotonic as determined by paired t-test).

To complement the results investigating strength and relative strength, we also quantified probability and relative probability for the hotspots after chemical triggers. We find that the probability of actin dynamics in hotspots within the boundary does not change for either stimulus ($p=0.969$ for control vs. high K^+ and $p=0.557$ for control vs. hypotonic as determined by paired t-test), though the probability of dynamics within bulk region hotspots significantly decreases after hypotonic challenge ($p=0.847$ for control vs. high K^+ and $p=0.027$ for control vs. hypotonic as determined by paired t-test). For both chemical triggers, there is no relative change in probability

within hotspots (p=0.215 for control vs. high K^+ and p=0.462 for control vs. hypotonic as determined by paired t-test).

To provide a static visualization of actin dynamics within these hotspots, we show traditional actin fluorescence kymographs (**Fig. 2C1**) and novel actin dynamics kymographs (**Fig. 2C2**) for the three largest hotspot regions (reg, orange, and yellow) in the representative cell. Both types of kymographs clearly show stronger dynamics in the triggering condition. Moreover, while not evident in the kymograph shown, we also find that cells triggered by high K^+ show a significant decrease in the number of hotspots (p=0.021 for control vs. high K^+ and p=0.189 for control vs. hypotonic; **Suppl. Fig. 2B3**) and a concomitant increase in the average area of hotspots (p=0.047 for control vs. high K^+ and p=0.794 for control vs. hypotonic; **Suppl. Fig. 2B4**), indicating that nearby hotspots may have merged in the high potassium environment. Taken together, these results show that i) hotspot regions respond differently to chemically triggering stimuli than does the subcellular region in which they reside (**Fig. 2B1-B2**) and ii) they are specifically reactive to the high K^+ chemical stimulus in terms of strength of dynamics and both number and average area of hotspots (**Suppl. Fig. 2B3-B4**).

<u>Astrocytes display distinct actin dynamics in the presence of neurons and nanotopographic cues</u>

To observe actin dynamics in more *in vivo*-like cell culture conditions, we used two different approaches: i) astrocytes plated on a nanostructured surface, with starlike shapes and more realistic molecular and functional features devoted to homeostatic control of potassium concentrations and cell volume [79,77], and ii) co-culture of astrocytes with primary cortical neurons.

For the first approach, we took advantage of the topographic features in hydrotalcyte-like compound (HTlc) films to understand how actin dynamics is altered by mechanical stimuli at the nanometer scale. For the second approach, we transduced primary astrocytes while still in the flask and then added them to cultures of primary neurons to generate a co-culture. The results shown in **Fig. 3** characterize how the actin dynamics of polygonal astrocytes grown on PDL-coated glass ("PDL" or "PDL cells") differ from differentiated astrocytes grown on the nanotopographic surface HTlc ("HTlc" or "HTlc cells") and from astrocytes co-cultured with neurons ("Co" or "Co cells") under control conditions (standard external medium). Representative examples of fluorescence overlays and optical flow analyses for each cell type are shown in **Fig. 3A**.

In **Fig. 3B,** we first compared how actin dynamics differs in the boundary and bulk regions for PDL cells, HTlc cells, and Co cells. We find that both PDL cells and Co cells show significantly stronger dynamics within the boundary region and within the bulk region compared to HTlc cells (**Fig. 3B1**; p<0.001 for HTlc vs. PDL and p<0.001 for HTlc vs. Co as determined by one-way ANOVA followed by Tukey's multiple comparisons test). Surprisingly though, when comparing boundary to bulk within each condition (**Fig. 3B2**), we find that all conditions (PDL, HTlc, and Co) show significantly stronger dynamics at the boundary compared to the bulk (p<0.001 for PDL, and p=0.012 for HTlc, and p=0.001 for Co as determined by paired t-test).

We next compared how likely the different groups of cells are to show actin dynamics in different subcellular regions. Within both the boundary and bulk regions, only Co cells are significantly more likely to show actin dynamics compared to PDL cells (**Fig. 3C1**; $p<0.001$ for boundary and $p=0.003$ for bulk as determined by one-way ANOVA followed by Tukey's multiple comparisons test). The probability of observing dynamics within the boundary and bulk of HTlc cells is not significantly different from either PDL or Co cells (boundary: $p=0.051$ for PDL vs. HTlc and $p=0.082$ for HTlc vs Co; bulk: $p=0.128$ for PDL vs HTlc and $p=0.604$ for HTlc vs Co; all as determined by one-way ANOVA followed by Tukey's multiple comparisons test). In this case, there is no significant difference between probability of dynamics within boundary and bulk for any condition (**Fig. 3C2**; $p=0.072$ for PDL, $p=0.615$ for HTlc, and $p=0.093$ for Co as determined by paired t-test).

Finally, we evaluated distance dependence of actin dynamics under each culturing condition in **Fig. 3D**. We show the full distance curves in **Suppl. Fig. 2C** for the representative cells. When comparing individual distances within boundary region (**Fig. 3D1**), we see that only Co cells are significantly more likely to have actin dynamics than PDL cells at specific distances ($p<0.001$ for all distances between 0.72 and 2.16 μm as determined by two-way ANOVA followed by Tukey's multiple comparisons test). Finally, when examining the fraction of events within the boundary (**Fig. 3D2**), we find that PDL cells are less likely to have actin dynamics within the boundary than either HTlc cells and Co cells ($p=0.031$ and $p<0.001$ for PDL vs. HTlc and for PDL vs. Co, respectively, as determined by one-way ANOVA followed by Tukey's multiple comparisons test), with no difference between HTlc and Co cells ($p=0.122$ as determined by one-way ANOVA followed by Tukey's multiple comparisons test). Taken together, these results indicate the following: i) HTlc cells show weaker actin dynamics than both PDL and Co cells with no difference in probability (**Fig. 3B1** and **Fig. 3C1**), ii) Co cells show equally strong and more frequent actin dynamics than PDL cells (**Fig. 3B1** and **Fig. 3C1**), and iii) both HTlc and Co cells show a significant shift in dynamics towards the boundary compared to PDL cells (**Fig. 3D2**).

<u>Astrocytes display hotspot regions in the presence of neurons that are more active than in the absence of neurons</u>

We next sought to compare whether hotspot dynamics differed between astrocytes cultured on PDL-coated glass in the absence of neurons (PDL) and in the presence of neurons (Co). Astrocytes grown and differentiated on HTlc did not display consistent hotspot regions for reliable analysis.

Within hotspots, the strength of actin dynamics within the boundary region is significantly stronger in Co cells compared to PDL cells, whereas we observe no difference between PDL and Co cells within the bulk region (**Fig. 4B1**; $p=0.003$ for PDL vs. Co within boundary and $p=0.063$ for PDL vs. Co within bulk as determined by two-sample t-test). Additionally, Co cells also show a significant increase in the strength of hotspot dynamics between the boundary and bulk (**Fig. 4B2**; $p=0.075$ for PDL and $p<0.001$ for Co as determined by paired t-tests). The relative strength of hotspots within Co cells is also significantly higher than within PDL cells (**Fig. 4B3**; $p=0.009$ as determined by two-sample t-test).

646 We next considered probability of dynamics within hotspots under different culturing conditions.
647 The probability of hotspot dynamics is significantly higher for Co cells compared to PDL cells,
648 both within the boundary and within the bulk (**Fig. 4C1**; $p<0.001$ for PDL vs. Co within
649 boundary and $p=0.001$ for PDL vs. Co within bulk as determined by two-sample t-test). Co cells
650 also show a significant increase in the probability of boundary over bulk hotspot dynamics
651 (**Fig. 4C2**; $p=0.051$ for PDL and $p=0.005$ for Co as determined by paired t-tests). Furthermore,
652 the average persistence of dynamics within the hotspots of Co cells is significantly higher than
653 that of PDL cells (**Fig. 4C3**; $p=0.001$ as determined by two-sample t-test).
654
655 Finally, the relative probability of dynamics is lower in Co cells than in PDL cells
656 (**Suppl. Fig. 2D1**; $p=0.011$ for PDL vs. Co as determined by two-sample t-test), indicating that
657 astrocytes co-cultured with neurons are generally more active than without neurons but that their
658 hotspots are less relatively active compared to astrocytes without neurons. The number of
659 hotspots does not differ between PDL cells and Co cells (**Suppl. Fig. 2D2**; $p=0.333$ for PDL vs.
660 Co as determined by two-sample t-test), but the average area of hotspots is increased in Co cells
661 (**Suppl. Fig. 2D3**; $p=0.021$ for PDL vs. Co as determined by two-sample t-test).
662
663 Taken together, we have shown that, when compared to primary astrocytes only, astrocytes co-
664 cultured with neurons have hotspot dynamics that i) are stronger and more frequent within the
665 boundary (**Fig. 4B1** and **Fig. 4C1**), ii) are relatively stronger (**Fig. 4B3**) but relatively less
666 frequent (**Fig. 4D1**), and iii) persist for longer (**Fig. 4C3**).
667
668 <u>Astrocytes sense nanotopographic cues through actin orientation near the boundary</u>
669
670 Inspired by our analysis of actin dynamics in live astrocytes, we sought to understand i) why
671 certain "hotspots" of actin activity are more prevalent in cells grown on PDL than in cells grown
672 on HTlc and ii) whether the characteristics of actin dynamics are related to the underlying actin
673 structure. To this end, we cultured primary rat astrocytes on PDL-coated glass or on HTlc films
674 and performed STED microscopy on fixed cells stained for F-actin and the intermediate filament
675 protein glial fibrillary acid protein (GFAP). Representative images are shown in **Fig. 5**. HTlc
676 preferentially induces stellate morphology characteristic of differentiated astrocytes, whereas
677 astrocytes cultured on PDL-coated glass display the polygonal shapes characteristic of
678 undifferentiated astrocytes grown in the absence of neurons [80-84,87,12,79]. We chose not to
679 use astrocytes co-cultured with neurons in this portion of our study because the density of the
680 resulting co-culture would have led to overlapping protrusions and therefore would have
681 prevented robust single-cell analysis.
682
683 Confocal images of F-actin labeled astrocytes reveal that there is a marked tendency for cells
684 grown on PDL (**Fig. 5A**) to display a polygonal and dynamic phenotype with distinct leading and
685 trailing edges and several motile structures (i.e. lamellipodia, filopodia, stress fibers; **Fig. 5C**).
686 Conversely, in the "star" shaped cells grown on HTlc (**Fig. 5B**), the same motile elements that
687 would indicate direction of propagation are not clearly visible (**Fig. 5D**). Moreover, the
688 astrocytic actin is seen to "burst" out of the actin cortex in HTlc cells (**Fig. 5D**). This bursting or
689 "flaring" behavior is indicative of a functional microdomain, known to be present in
690 differentiated astrocytes grown on HTlc [79]. Although many regions in the representative HTlc
691 cell display this microdomain morphology, the actin dynamics of astrocytes plated on HTlc is of

692 lower magnitude than that of astrocytes grown on PDL (refer to **Fig. 3B**). Therefore, we chose to
693 investigate how astrocytic actin senses the different mechanical environments presented by PDL-
694 coated glass and HTlc films and analyze the subsequent cytoskeleton remodeling at a nanoscale
695 level via superresolution imaging. We used a method for quantitative, semi-automated analysis
696 of the actin bundles' preferential orientation [107] to assess the involvement of actin
697 organization in sensing the local mechanical environment around astrocytes.
698
699 Image analysis was performed by combining segmentation via an anisotropic, rotating Laplacian
700 of gaussian (LoG) kernel with a hierarchical cluster analysis (see **Fig. 6A** for a schematic
701 overview and *Materials and Methods* for a detailed description). These image processing
702 techniques allow for the analysis of actin angle organization and the determination of fractions of
703 actin roughly parallel versus roughly perpendicular to the leading edge of the cell boundary
704 (**Fig. 6B**). From our clustered data, we determine that PDL astrocytic actin is oriented more
705 parallel relative to the leading edge of the astrocyte, whereas HTlc astrocytic actin is oriented
706 more perpendicular (**Fig. 6C**). The difference seen between the actin of cells grown on PDL
707 versus on HTlc is significant as the cluster algorithm identifies two clusters within the data.
708 Moreover, we see the cluster groups largely correspond with the chosen nanotopography, with an
709 error of seven out of 37 cells: one HTlc cell is misclustered, and six PDL cells are misclustered
710 (i.e., six PDL cells can be found in the cluster of predicted HTlc actin fractions). While the
711 differences observed between astrocytes grown on HTlc and those grown on PDL at a dynamic,
712 micron scale do not necessarily correspond to the differences seen in structure at the nanometer
713 scale, our analytical approach reveals that the underlying nanoscale organization of actin within
714 astrocytes does indeed change when the cells are exposed to different nanotopographic surfaces.
715 Future work will optimize our co-culture approach and determine how the nanoscale structure of
716 astrocytic actin changes when astrocytes are in contact with neurons.
717
718
719 **Discussion**
720
721 We show, for the first time, by means of live timelapse confocal microscopy, that astrocytes
722 respond to alterations in the chemophysical environment with changes in actin dynamics.
723 Furthermore, we demonstrate that actin is spatiotemporally organized into micron scale
724 territories where the dynamics are enhanced depending on the specific chemophysical stress or
725 environment (topography or co-culture). Finally, we show how distinct organization of actin near
726 the boundary may contribute to dynamics.
727
728 Our study reveals that actin dynamics occurs persistently and locally, with actin dynamics
729 detectable near the boundary even when the boundary itself does not shift measurably.
730 Hypotonic challenge increases the strength of actin dynamics while high potassium preferentially
731 increases the strength of hotspot dynamics, both within the boundary region. Furthermore, while
732 astrocytes do not change shape substantially on the short timescales of our experiments, we see
733 small filopodial and lamellopodial structures – the F-actin-rich subcellular compartments of
734 migrating non-neuronal cells [108] – near the cell boundary that appear to "idle" by rapidly
735 extending and retracting, effectively sampling their local environment. It is in these regions,
736 which tend to lack strong stress fibers, that we most often observe actin dynamics. In future
737 experiments, we will quantify how local actin dynamics contribute to changes in astrocyte

morphology that occur during differentiation or after injury. Indeed, many studies have extensively demonstrated that, on longer timescales, astrocytes are extremely plastic cells. For example, astrocytes change their morphology by becoming polarized and growing long processes after severe tissue damage caused by traumatic injuries [109-111] and also become hypertrophic and lose their fine processes when they become reactive [112,19].

Surprisingly, dynamics are stronger in astrocytes grown on flat surfaces (PDL-coated glass) and when astrocytes are co-cultured with neurons, clustering into hotspot regions, whereas they are weaker in cells grown on nanostructured surfaces (HTlc films) and do not cluster into large enough regions for hotspot dynamics to be detected with confocal microscopy. Dynamic hotspots in differentiated astrocytes might present as miniature versions of lamellipodia and filopodia, and future work will use higher magnification imaging to determine if this is indeed the case. Importantly, the co-culture results demonstrate that actin dynamics is not highly sensitive to plating density because the co-culture plates were higher in density than the plates with astrocytes only (whether cultured on PDL or HTlc).

Our STED data might also provide the key to understanding why polygonal astrocytes display more robust cytoskeleton dynamics: a more parallel and dispersed organization of actin fibers into a meshwork underneath the cell membrane is likely to confer mechanical plasticity to the plasma membrane compared to differentiated cells grown on HTLc, where actin fibers are packed into "actin rails" and not only maintain the cell shape (especially in the cellular processes) but also might cause membrane stiffness or resistance to motility. In support of our hypothesis, a recent study demonstrated increased stiffness at the leading edge of migrating astrocytes using live STED and atomic force microscopy [113]. We also hypothesize that this distinct actin structure will lead to differences in the interaction with neighboring cells. As stellation enables communication with other cell types, perpendicular actin may ensure processes are directed along the proper axis for communication. Indeed, recent work implicates membrane-bound integrins, specifically astrocytic integrin-engaged Thy1, in interacting with the neuronal cytoskeleton to promote astrocyte-neuron communication [114]. Moreover, our finding that almost all cells cultured on HTlc have actin structures perpendicular to the boundary affirms the ability of HTlc to encourage stellate morphology and differentiation of astrocytes [79]. Our analysis also hints that some cells grown on PDL have actin structures that "look" like the actin structures of stellate, differentiated cells grown on HTlc, consistent with previous observations that growth of astrocytes on PDL delays but does not fully suppress spontaneous or gliotic differentiation that might occur in standard cell culture [48,79,115,116].

Previous studies demonstrated that astrocytes grown on HTlc are more efficient in their homeostatic process. In particular, the expression and function of Kir4.1 and water channel aquaporin 4 (AQP4) as well as the functional response to anisotonic challenge are enhanced in differentiated [77,79] and mature [117-122] cells. A more efficient response to homeostatic challenges due to the higher levels of channel proteins may be related to the weaker actin dynamics observed in differentiated cells compared to polygonal cells (both with and without neurons). While we have not directly investigated this question, a direct relationship between channel function and cytoskeleton dynamics would not be surprising, if we consider that astrocytes may harness the excitable dynamics of actin to codify and convey information coming from the extracellular milieu. Indeed, in fixed cells, it has been shown that the actin cytoskeleton

784 affects AQP4 localization [47,123], but how real time actin dynamics affects the localization and
785 function of AQP4 and other channels, including Kir4.1, remains unknown. To this end, future
786 work will reveal whether the function of potassium and water channels is altered in differentiated
787 compared to polygonal astrocytes after homeostatic challenge and whether any differences in
788 channel localization and function are directly tied to the dynamic response of actin.
789
790 Much is known about how co-culturing astrocytes with neurons alters neuronal function [124-
791 127], but how are astrocytes affected by the presence of neurons? Several studies have shown
792 that the presence of neurons and neuronal activity controls gene expression in
793 astrocytes [128,80,129] and affects astrocytic calcium dynamics [130,131]. For example, rat
794 cortical astrocytes express glutamate-aspartate transporter (GLAST), but in the presence of
795 cortical neurons, as we have done here, astrocytes also express glutamate transporter-1 (GLT-
796 1) [129,80]. Neurons have also been shown to enhance astrocytic expression of Cx43, gap
797 junctional communication between astrocytes, and the propagation of calcium waves within the
798 astrocytic network [132]. We hypothesize that actin dynamics in astrocytes co-cultured with
799 neurons is enhanced specifically because actin dynamics contributes to astrocytes' critical
800 function of facilitating neuronal activity by interacting with neurons and sensing the extracellular
801 environment. Recent work has indicated that actin-dependent morphology changes in PAPs are
802 not only critical for interacting with neurons but may also enhance spine stability [133]. Future
803 work will probe more deeply into how astrocytic actin dynamics affects the functional dynamics
804 of astrocyte-neuron networks.
805
806 These questions remain to be elucidated, and studies in microglia [53] – which demonstrated that
807 actin dynamics is critical for their principal function, surveillance – indicate that actin dynamics
808 also plays an important role *in vivo* in neural cells. We propose that actin dynamics in astrocytes
809 is critical for astrocytes' principal functions: maintaining homeostasis and modulating neuronal
810 communication. Finally, given that cytoskeletal alterations are reported in a variety of
811 neurological conditions characterized by a gliotic state [134], we expect investigations of
812 cytoskeletal dynamics in defined animal models to be an important area of exploration to
813 validate the pathophysiological relevance [135] of our findings.
814
815 Moreover, while we know that the astrocyte-neuron interactions will happen on a spatial scale
816 much smaller than the dynamics observed here, our hypothesis is supported by a recent study
817 highlighting the importance of mechanical signaling for synaptic activity [54]. We therefore
818 intuit that astrocytic actin dynamics may serve as a mechanical regulator of neuronal activity.
819
820 **References**

821 1. Scemes E, Spray DC (2012) Extracellular K^+ and astrocyte signaling via connexin and
822 pannexin channels. Neurochemical research 37 (11):2310-2306. doi:10.1007/s11064-012-0759-4

823 2. Somjen GG (1979) Extracellular potassium in the mammalian central nervous system. Annu
824 Rev Physiol 41:159-177. doi:10.1146/annurev.ph.41.030179.001111

825 3. Walz W (1987) Swelling and potassium uptake in cultured astrocytes. Can J Physiol
826 Pharmacol 65 (5):1051-1057. doi:10.1139/y87-166

827 4. Kofuji P, Newman EA (2004) Potassium buffering in the central nervous system.
828 Neuroscience 29 (4):1045-1056. doi:10.1016/j.neuroscience.2004.06.008

829 5. Holthoff K, Witte OW (2000) Directed spatial potassium redistribution in rat neocortex. Glia
830 29(3): (3):288-292. doi:10.1002/(sici)1098-1136(20000201)29:3<288::aid-glia10>3.0.co;2-8

831 6. Orkand RK, Nicholls JG, Kuffler SW (1966) Effect of nerve impulses on the membrane
832 potential of glial cells in the central nervous system of amphibia. J Neurophysiol 29 (4):788-806.
833 doi:10.1152/jn.1966.29.4.788

834 7. Kuffler SW, Nicholls JG, Orkand RK (1966) Physiological properties of glial cells in the
835 central nervous system of amphibia. J Neurophysiol 29 (4):768-787.
836 doi:10.1152/jn.1966.29.4.768

837 8. Baylor DA, Nicholls JG (1969) Changes in extracellular potassium concentration produced by
838 neuronal activity in the central nervous system of the leech. J Physiol 203 (3):555-569.
839 doi:10.1113/jphysiol.1969.sp008879

840 9. Berger T, Schnitzer J, Kettenmann H (1991) Developmental changes in the membrane current
841 pattern, K+ buffer capacity, and morphology of glial cells in the corpus callosum slice. J
842 Neurosci 11 (10):3008-3024. doi:10.1523/JNEUROSCI.11-10-03008.1991

843 10. Newman EA (1986) Regional specialization of the membrane of retinal glial cells and its
844 importance to K+ spatial buffering. Ann N Y Acad Sci 481:273-286. doi:10.1111/j.1749-
845 6632.1986.tb27158.x

846 11. Walz W, Wuttke W, Hertz L (1984) Astrocytes in primary cultures: membrane potential
847 characteristics reveal exclusive potassium conductance and potassium accumulator properties.
848 Brain Res 292 (2):367-374. doi:10.1016/0006-8993(84)90772-8

849 12. Benfenati V, Caprini M, Nobile M, Rapisarda C, Ferroni S (2006) Guanosine promotes the
850 up-regulation of inward rectifier potassium current mediated by Kir4.1 in cultured rat cortical
851 astrocytes. J Neurochem 98 (2):430-445. doi:10.1111/j.1471-4159.2006.03877.x

852 13. Parpura V, Verkhratsky A (2012) Neuroglia at the crossroads of homoeostasis, metabolism
853 and signalling: evolution of the concept. ASN Neuro 4 (4):e00087. doi:10.1042/AN20120019

854 14. Benfenati V, Ferroni S (2010) Water transport between CNS compartments: Functional and
855 molecular interactions between aquaporins and ion channels. Neuroscience 168 (4):926-940.
856 doi:10.1016/j.neuroscience.2009.12.017

857 15. Amiry-Moghaddam M, Ottersen OP (2003) The molecular basis of water transport in the
858 brain. Nature reviews 4 (12):991-1001. doi:10.1038/nrn1252

859 16. Bellot-Saez A, Kékesi O, Morley JW, Buskila Y (2017) Astrocytic modulation of neuronal
860 excitability through K+ spatial buffering. Neuroscience and biobehavioral reviews 77:87-97.
861 doi:10.1016/j.neubiorev.2017.03.002

862 17. Oberheim NA, Goldman SA, Nedergaard M (2012) Heterogeneity of astrocytic form and
863 function. Methods Mol Biol 814: 23–45:23-45. doi:10.1007/978-1-61779-452-0_3

864 18. Bushong EA, Martone ME, Jones YZ, Ellisman MH (2002) Protoplasmic astrocytes in CA1
865 stratum radiatum occupy separate anatomical domains. J Neurosci 22 (1):183-192.
866 doi:10.1523/JNEUROSCI.22-01-00183.2002

867 19. Schiweck J, Eickholt BJ, Murk K (2018) Important shapeshifter: Mechanisms allowing
868 astrocytes to respond to the changing nervous system during development, injury and disease.
869 Front Cell Neurosci 12:261. doi:10.3389/fncel.2018.00261

870 20. Boulay AC, Saubaméa B, Adam N, Chasseigneaux S, Mazaré N, Gilbert A, Bahin M,
871 Bastianelli L, Blugeon C, Perrin S, Pouch J, Ducos B, Le Crom S, Genovesio A, Chrétien F,
872 Declèves X, Laplanche JL, Cohen-Salmon M (2017) Translation in astrocyte distal processes
873 sets molecular heterogeneity at the gliovascular interface. Cell Discov 3:17005.
874 doi:10.1038/celldisc.2017.5

875 21. Yang Y, Gozen O, Watkins A, Lorenzini I, Lepore A, Gao Y, Vidensky S, Brennan J,
876 Poulsen D, Park JW, Jeon NL, Robinson MB, Rothstein JD (2009) Presynaptic regulation of
877 astroglial excitatory neurotransmitter transporter GLT1. Neuron 61 (6):880-894.
878 doi:10.1016/j.neuron.2009.02.010

879 22. Sibille J, Pannasch U, Rouach N (2014) Astroglial potassium clearance contributes to short-
880 term plasticity of synaptically evoked currents at the tripartite synapse. J Physiol 592 (1):87-102.
881 doi:10.1113/jphysiol.2013.261735

882 23. Murphy-Royal C, Dupuis J, Groc L, Oliet SHR (2017) Astroglial glutamate transporters in
883 the brain: Regulating neurotransmitter homeostasis and synaptic transmission. J Neurosci Res 95
884 (11):2140-2151. doi:10.1002/jnr.24029

885 24. Dallérac G, Zapata J, Rouach N (2018) Versatile control of synaptic circuits by astrocytes:
886 where, when and how? Nature reviews 19 (12):729-743. doi:10.1038/s41583-018-0080-6

887 25. Mazaré N, Oudart M, Cohen-Salmon M (2021) Local translation in perisynaptic and
888 perivascular astrocytic processes - a means to ensure astrocyte molecular and functional polarity?
889 J Cell Sci 134 (2):jcs251629. doi:10.1242/jcs.251629

890 26. Ghézali G, Dallérac G, Rouach N (2016) Perisynaptic astroglial processes: dynamic
891 processors of neuronal information. Brain Struct Funct 221:2427-2442

892 27. Spray DC (1996) Molecular physiology of gap junction channels. Clin Exp Pharmacol
893 Physiol 23 (12):1038-1040. doi:10.1111/j.1440-1681.1996.tb01165.x

894 28. De Pina-Benabou MH, Srinivas M, Spray DC, Scemes E (2001) Calmodulin kinase pathway
895 mediates the K+-induced increase in Gap junctional communication between mouse spinal cord
896 astrocytes. J Neurosci 21 (17):6635-6643. doi:10.1523/JNEUROSCI.21-17-06635.2001

897 29. Giaume C, Tabernero A, Medina JM (1997) Metabolic trafficking through astrocytic gap
898 junctions. Glia 21 (1):114-123

899 30. Venance L, Piomelli D, Glowinski J, Giaume C (1995) Inhibition by anandamide of gap
900 junctions and intercellular calcium signalling in striatal astrocytes. Nature 376 (6541):590-594.
901 doi:10.1038/376590a0

902 31. Finkbeiner S (1992) Calcium waves in astrocytes-filling in the gaps. Neuron 8 (6):1101-
903 1108. doi:10.1016/0896-6273(92)90131-v

904 32. Enkvist MO, McCarthy KD (1992) Activation of protein kinase C blocks astroglial gap
905 junction communication and inhibits the spread of calcium waves. J Neurochem 59 (2):519-526.
906 doi:10.1111/j.1471-4159.1992.tb09401.x

907 33. Murphy TH, Blatter LA, Wier WG, Baraban JM (1993) Rapid communication between
908 neurons and astrocytes in primary cortical cultures. J Neurosci 13(6): (6):2672-2679.
909 doi:10.1523/JNEUROSCI.13-06-02672.1993

910 34. Charvériat M, Naus CC, Leybaert L, Sáez JC, Giaume C (2017) Connexin-dependent
911 neuroglial networking as a new therapeutic target. Front Cell Neurosci 11:174.
912 doi:10.3389/fncel.2017.00174

913 35. Verkhratsky A, Nedergaard M (2017) Physiology of Astroglia. Physiol Rev 98 (1):239-389.
914 doi:10.1152/physrev.00042.2016

915 36. Rose CR, Verkhratsky A (2016) Principles of sodium homeostasis and sodium signalling in
916 astroglia. Glia 64 (10):1611-1627. doi:10.1002/glia.22964

917 37. Santello M, Toni N, Volterra A (2019) Astrocyte function from information processing to
918 cognition and cognitive impairment. Nat Neurosci 22 (2):154-166. doi:10.1038/s41593-018-
919 0325-8

920 38. Farhy-Tselnicker I, Boisvert MM, Liu H, Dowling C, Erikson GA, Blanco-Suarez E, Farhy
921 C, Shokhirev MN, Ecker JR, Allen NJ (2021) Activity-dependent modulation of synapse-
922 regulating genes in astrocytes. Elife 10:e70514. doi:10.7554/eLife.70514

923 39. Ramakers GJ, Moolenaar WH (1998) Regulation of astrocyte morphology by RhoA and
924 lysophosphatidic acid. Experimental cell research 245 (2):252-262. doi:10.1006/excr.1998.4224.

925 40. Kalman D, Gomperts SN, Hardy S, Kitamura M, Bishop JM (1999) Ras family GTPases
926 control growth of astrocyte processes. Mol Biol Cell 10 (5):1665-1683.
927 doi:10.1091/mbc.10.5.1665

928 41. John GR, Chen L, Rivieccio MA, Melendez-Vasquez CV, Hartley A, Brosnan CF (2004)
929 Interleukin-1beta induces a reactive astroglial phenotype via deactivation of the Rho GTPase-
930 Rock axis. J Neurosci 24 (11):2837-2845. doi:10.1523/JNEUROSCI.4789-03.2004

931 42. Höltje M, Hoffmann A, Hofmann F, Mucke C, Grosse G, Van Rooijen N, Kettenmann H,
932 Just I, Ahnert-Hilger G (2005) Role of Rho GTPase in astrocyte morphology and migratory
933 response during in vitro wound healing. J Neurochem 95 (5):1237-1248. doi:10.1111/j.1471-
934 4159.2005.03443.x

935 43. Racchetti G, D'Alessandro R, Meldolesi J (2012) Astrocyte stellation, a process dependent on
936 Rac1 is sustained by the regulated exocytosis of enlargeosomes. Glia 60 (3):465-475.
937 doi:10.1002/glia.22280

938 44. Suidan HS, Nobes CD, Hall A, Monard D (1997) Astrocyte spreading in response to
939 thrombin and lysophosphatidic acid is dependent on the Rho GTPase. Glia 21 (2):244-252.
940 doi:10.1002/(sici)1098-1136(199710)21:2<244::aid-glia7>3.0.co;2-6

941 45. Murk K, Blanco Suarez EM, Cockbill LMR, Banks P, Hanley JG (2013) The antagonistic
942 modulation of Arp2/3 activity by N-WASP, WAVE2 and PICK1 defines dynamic changes in
943 astrocyte morphology. J Cell Sci 126 (17):3873-3883. doi:10.1242/jcs.125146

944 46. Brozzi F, Arcuri C, Giambanco I, Donato R (2009) S100B Protein Regulates Astrocyte
945 Shape and Migration via Interaction with Src Kinase: IMPLICATIONS FOR ASTROCYTE
946 DEVELOPMENT, ACTIVATION, AND TUMOR GROWTH. J Biol Chem 284 (13):8797-
947 8811. doi:10.1074/jbc.M805897200

948 47. Nicchia GP, Rossi A, Mola MG, Procino G, Frigeri A, Svelto M (2008) Actin cytoskeleton
949 remodeling governs aquaporin-4 localization in astrocytes. Glia 56 (16):1755-1766.
950 doi:10.1002/glia.20724

951 48. Benfenati V, Nicchia GP, Svelto M, Rapisarda C, Frigeri A, Ferroni S (2007) Functional
952 down-regulation of volume-regulated anion channels in AQP4 knockdown cultured rat cortical
953 astrocytes. Journal of Neurochemistry 100 (1):87-104. doi:10.1111/j.1471-4159.2006.04164.x

954 49. Nicchia GP, Mola MG, Pisoni M, Frigeri A, Svelto M (2007) Different pattern of aquaporin-
955 4 expression in extensor digitorum longus and soleus during early development. Muscle Nerve
956 35 (5):625-631. doi:10.1002/mus.20736

957 50. Fritzsche M, Fernandes RA, Chang VT, Colin-York H, Clausen MP, Felce JH, Galiani S,
958 Erlenkämper C, Santos AM, Heddleston JM, Pedroza-Pacheco I, Waithe D, de la Serna JB,
959 Lagerholm BC, Liu T-L, Chew T-L, Betzig E, Davis SJ, Eggeling C (2017) Cytoskeletal actin
960 dynamics shape a ramifying actin network underpinning immunological synapse formation.
961 Science advances 3 (6):e1603032. doi:10.1126/sciadv.1603032

962 51. Li X, Miao Y, Pal DS, Devreotes PN (2020) Excitable networks controlling cell migration
963 during development and disease. Semin Cell Dev Biol 100:133-142.
964 doi:10.1016/j.semcdb.2019.11.001

965 52. Kumari S, Mak M, Poh YC, Tohme M, Watson N, Melo M, Janssen E, Dustin M, Geha R,
966 Irvine DJ (2020) Cytoskeletal tension actively sustains the migratory T-cell synaptic contact.
967 EMBO J 39 (5):e102783. doi:10.15252/embj.2019102783

968 53. Bernier L-P, Bohlen CJ, York EM, Choi HB, Kamyabi A, Dissing-Olesen L, Hefendehl JK,
969 Collins HY, Stevens B, Barres BA, MacVicar BA (2019) Nanoscale surveillance of the brain by
970 microglia via cAMP-regulated filopodia. Cell Rep 27 (10):2895-2908.e2894.
971 doi:10.1016/j.celrep.2019.05.010

972 54. Ucar H, Watanabe S, Noguchi J, Morimoto Y, Iino Y, Yagishita S, Takahashi N, Kasai H
973 (2021) Mechanical actions of dendritic-spine enlargement on presynaptic exocytosis. Nature 600
974 (7890):686-689. doi:10.1038/s41586-021-04125-7

975 55. Vicker MG (2002) F-actin assembly in Dictyostelium cell locomotion and shape oscillations
976 propagates as a self-organized reaction-diffusion wave. FEBS Letters 510 (1-2):5-9.
977 doi:10.1016/s0014-5793(01)03207-0

978 56. Sun X, Driscoll MK, Guven C, Das S, Parent CA, Fourkas JT, Losert W (2015) Asymmetric
979 nanotopography biases cytoskeletal dynamics and promotes unidirectional cell guidance. Proc
980 Natl Acad Sci U S A 112 (41):12557-12562. doi:10.1073/pnas.1502970112

981 57. Driscoll MK, Sun X, Guven C, Fourkas JT, Losert W (2014) Cellular contact guidance
982 through dynamic sensing of nanotopography. ACS Nano 8 (4):3546-3555.
983 doi:10.1021/nn406637c

984 58. Edwards M, Cai H, Abubaker-Sharif B, Long Y, Lampert TJ, Devreotes PN (2018) Insight
985 from the maximal activation of the signal transduction excitable network in Dictyostelium
986 discoideum. Proc Natl Acad Sci U S A 115 (16):E3722-E3730. doi:10.1073/pnas.1710480115

987 59. Miao Y, Bhattacharya S, Banerjee T, Abubaker-Sharif B, Long Y, Inoue T, Iglesias PA,
988 Devreotes PN (2019) Wave patterns organize cellular protrusions and control cortical dynamics.
989 Mol Syst Biol 15 (3):e8585. doi:10.15252/msb.20188585

990 60. Lee R, Campanello L, Hourwitz M, Alvarez P, Omidvar A, Fourkas J, Losert W (2020)
991 Quantifying topography-guided actin dynamics across scales using optical flow. Mol Biol Cell
992 mbcE19110614. doi:10.1091/mbc.E19-11-0614

993 61. Roy S (2016) Waves, rings, and trails: The scenic landscape of axonal actin. J Cell Biol 212
994 (2):131-134. doi:10.1083/jcb.201511016

995 62. Del Signore SJ, Kelley CF, Messelaar EM, Lemos T, Marchan MF, Ermanoska B, Mund M,
996 Fai TG, Kaksonen M, Rodal AA (2021) An autoinhibitory clamp of actin assembly constrains
997 and directs synaptic endocytosis. Elife 10:e69597. doi:10.7554/eLife.69597

998 63. Bull AL, Campanello L, Hourwitz MJ, Yang Q, Zhao M, Fourkas JT, Losert W (2022) Actin
999 dynamics as a multiscale integrator of cellular guidance cues. Front Cell Dev Biol 10:873567.
1000 doi:10.3389/fcell.2022.873567

1001 64. Yang Q, Miao Y, Campanello LJ, Hourwitz MJ, Abubaker-Sharif B, Bull AL, Devreotes PN,
1002 Fourkas JT, Losert W (2022) Cortical waves mediate the cellular response to electric fields. Elife
1003 11:e73198. doi:10.7554/eLife.73198

1004 65. Pal DS, Li X, Banerjee T, Miao Y, Devreotes PN (2019) The excitable signal transduction
1005 networks: movers and shapers of eukaryotic cell migration. Int J Dev Biol 63 (8-9-10):407-416.
1006 doi:10.1387/ijdb.190265pd

1007 66. Horn BKP, Schunck BG (1981) Determining optical flow. Artif Intell 17:185-203

1008 67. Driscoll MK, Losert W, Jacobson K, Kapustina M (2015) Spatiotemporal relationships
1009 between the cell shape and the actomyosin cortex of periodically protruding cells. Cytoskeleton
1010 (Hoboken) 72 (6):268-281. doi:10.1002/cm.21229

1011 68. Driscoll MK, McCann C, Kopace R, Homan T, Fourkas JT, Parent C, Losert W (2012) Cell
1012 shape dynamics: from waves to migration. PLoS Comput Biol 8 (3):e1002392.
1013 doi:10.1371/journal.pcbi.1002392

1014 69. Du M, Li J, Wang R, Wu Y (2016) The influence of potassium concentration on epileptic
1015 seizures in a coupled neuronal model in the hippocampus. Cogn Neurodyn 10 (5):405-414.
1016 doi:10.1007/s11571-016-9390-4

1017 70. Pivonkova H, Hermanova Z, Kirdajova D, Awadova T, Malinsky J, Valihrach L, Zucha D,
1018 Kubista M, Galisova A, Jirak D, Anderova M (2018) The contribution of TRPV4 channels to
1019 astrocyte volume regulation and brain edema formation. Neuroscience 394:127-143.
1020 doi:10.1016/j.neuroscience.2018.10.028

1021 71. Kimelberg HK, Rutledge E, Goderie S, Charniga C (1995) Astrocytic swelling due to
1022 hypotonic or high K+ medium causes inhibition of glutamate and aspartate uptake and increases
1023 their release. Journal of cerebral blood flow and metabolism : official journal of the International
1024 Society of Cerebral Blood Flow and Metabolism 15 (3):409-416. doi:10.1038/jcbfm.1995.51

1025 72. O'Connor ER, Kimelberg HK, Keese CR, Giaever I (1993) Electrical resistance method for
1026 measuring volume changes in monolayer cultures applied to primary astrocyte cultures. Am J
1027 Physiol 264 (2 Pt 1):C471-478. doi:10.1152/ajpcell.1993.264.2.C471

1028 73. Dallwig R, Vitten H, Deitmer JW (2000) A novel barium-sensitive calcium influx into rat
1029 astrocytes at low external potassium. Cell Calcium 28(4): (4):247-259.
1030 doi:10.1054/ceca.2000.0153

1031 74. Yaguchi T, Nishizaki T (2010) Extracellular high K+ stimulates vesicular glutamate release
1032 from astrocytes by activating voltage-dependent calcium channels. J Cell Physiol 225 (2):512-
1033 518. doi:10.1002/jcp.22231

1034 75. O'Connor ER, Kimelberg HK (1993) Role of calcium in astrocyte volume regulation and in
1035 the release of ions and amino acids. J Neurosci 13 (6):2638-2650. doi:10.1523/JNEUROSCI.13-
1036 06-02638.1993

1037 76. Pangrsic T, Potokar M, Haydon PG, Zorec R, Kreft M (2006) Astrocyte swelling leads to
1038 membrane unfolding, not membrane insertion. J Neurochem 99 (2):514-523. doi:10.1111/j.1471-
1039 4159.2006.04042.x

1040 77. Mola MG, Saracino E, Formaggio F, Amerott AG, Barile B, Frigeri A, Palazzo C, Posati T,
1041 Zamboni R, Caprini M, Nicchia GP, Benfenati V (2021) Cell volume regulation mechanisms in
1042 differentiated astrocytes. Cell Physiol Biochem 55 (S1):196-212. doi:10.33594/000000469

1043 78. Mola MG, Sparaneo A, Gargano CD, Spray DC, Svelto M, Frigeri A, Scemes E, Nicchia GP
1044 (2016) The speed of swelling kinetics modulates cell volume regulation and calcium signaling in
1045 astrocytes: A different point of view on the role of aquaporins. Glia 64(1):139-54 (1):139-154.
1046 doi:10.1002/glia.22921

1047 79. Posati T, Pistone A, Saracino E, Formaggio F, Mola MG, Troni E, Sagnella A, Nocchetti M,
1048 Barbalinardo M, Valle F, Bonetti S, Caprini M, Nicchia GP, Zamboni R, Muccini M, Benfenati
1049 V (2016) A nanoscale interface promoting molecular and functional differentiation of neural
1050 cells. Sci Rep 6:31226. doi:10.1038/srep31226

1051 80. Swanson RA, Liu J, Miller JW, Rothstein JD, Farrell K, Stein BA, Longuemare MC (1997)
1052 Neuronal regulation of glutamate transporter subtype expression in astrocytes. J Neurosci 17
1053 (3):932-940. doi:10.1523/JNEUROSCI.17-03-00932.1997

1054 81. Sensenbrenner M, Labourdette G, Delaunoy JP, Pettmann B, Devilliers G, Moonen G, Bock
1055 E (1980) Morphological and biochemical differentiation of glial cells in primary culture. In:
1056 Giacobini E (ed) Tissue culture in neurobiology. Raven, New York, pp 385-395

1057 82. Pettmann B, Louis JC, Sensenbrenner M (1979) Morphological and biochemical maturation
1058 of neurones cultured in the absence of glial cells. Nature 281 (5730):378-380.
1059 doi:10.1038/281378a0

1060 83. Hertz L, Juurlink BHJ, Szuchet S (1985) Cell cultures. In: Lajtha A (ed) Handbook of
1061 neurochemistry, vol 8. 2 edn. Plenum, New York, pp 603-661

1062 84. Juurlink BH, Hertz L (1985) Plasticity of astrocytes in primary cultures: an experimental tool
1063 and a reason for methodological caution. Dev Neurosci 7 (5-6):263-277. doi:10.1159/000112295

1064 85. McCarthy KD, de Vellis J (1980) Preparation of separate astroglial and oligodendroglial cell
1065 cultures from rat cerebral tissue. J Cell Biol 85 (3):890-902. doi:10.1083/jcb.85.3.890

1066 86. Benfenati V, Toffanin S, Capelli R, Camassa LMA, Ferroni S, Kaplan DL, Omenetto FG,
1067 Muccini M, Zamboni R (2010) A silk platform that enables electrophysiology and targeted drug

1068 delivery in brain astroglial cells. Biomaterials 31 (31):7883-7891.
1069 doi:10.1016/j.biomaterials.2010.07.013

1070 87. Ferroni S, Marchini C, Schubert P, Rapisarda C (1995) Two distinct inwardly rectifying
1071 conductances are expressed in long term dibutyryl-cyclic-AMP treated rat cultured cortical
1072 astrocytes. FEBS Lett 367 (3):319-325. doi:10.1016/0014-5793(95)00588-z

1073 88. Saracino E, Maiolo L, Polese D, Semprini M, Borrachero-Conejo AI, Gasparetto J, Murtagh
1074 S, Sola M, Tomasi L, Valle F, Pazzini L, Formaggio F, Chiappalone M, Hussain S, Caprini M,
1075 Muccini M, Ambrosio L, Fortunato G, Zamboni R, Convertino A, Benfenati V (2020) A Glial-
1076 Silicon Nanowire Electrode Junction Enabling Differentiation and Noninvasive Recording of
1077 Slow Oscillations from Primary Astrocytes. Adv Biosyst 4 (4):e1900264.
1078 doi:10.1002/adbi.201900264

1079 89. Benfenati V, Ferroni S (2015) Microdynamics of Water and Ion Homeostasis in the Brain:
1080 Role of Aquaporins and Ion Channels of Astroglial Cells. In: Boison D, Masino SA (eds)
1081 Homeostatic Control of Brain Function. Oxford University Press.
1082 doi:10.1093/med/9780199322299.003.0001

1083 90. Benfenati V, Martino N, Antognazza MR, Pistone A, Toffanin S, Ferroni S, Lanzani G,
1084 Muccini M (2014) Photostimulation of whole-cell conductance in primary rat neocortical
1085 astrocytes mediated by organic semiconducting thin films. Adv Healthc Mater 3 (3):392-399.
1086 doi:10.1002/adhm.201300179

1087 91. Borrachero-Conejo AI, Adams WR, Saracino E, Mola MG, Wang M, Posati T, Formaggio F,
1088 De Bellis M, Frigeri A, Caprini M, Hutchinson MR, Muccini M, Zamboni R, Nicchia GP,
1089 Mahadevan-Jansen A, Benfenati V (2020) Stimulation of water and calcium dynamics in
1090 astrocytes with pulsed infrared light. FASEB journal : official publication of the Federation of
1091 American Societies for Experimental Biology 34 (5):6539-6553. doi:10.1096/fj.201903049R

1092 92. Firestein BL, Brenman JE, Aoki C, Sanchez-Perez AM, El-Husseini AE, Bredt DS (1999)
1093 Cypin: A cytosolic regulator of PSD-95 postsynaptic targeting. Neuron 24 (3):659-672.
1094 doi:10.1016/s0896-6273(00)81120-4

1095 93. O'Neill KM, Donohue KE, Omelchenko A, Firestein BL (2018) The 3' UTRs of Brain-
1096 Derived Neurotrophic Factor transcripts differentially regulate the dendritic arbor. Front Cell
1097 Neurosci 12:60. doi:10.3389/fncel.2018.00060

1098 94. O'Neill KM, Akum BF, Dhawan ST, Kwon M, Langhammer CG, Firestein BL (2015)
1099 Assessing effects on dendritic arborization using novel Sholl analyses. Frontiers in Cellular
1100 Neuroscience 9:285. doi:10.3389/fncel.2015.00285

1101 95. O'Neill KM, Kwon M, Donohue KE, Firestein BL (2017) Distinct effects on the dendritic
1102 arbor occur by microbead versus bath administration of brain-derived neurotrophic factor.
1103 Cellular and Molecular Life Sciences 74 (23):4369-4385. doi:10.1007/s00018-017-2589-7

1104 96. Rodriguez AR, O'Neill KM, Swiatkowski P, Patel MV, Firestein BL (2018) Overexpression
1105 of cypin alters dendrite morphology, single neuron activity, and network properties via distinct
1106 mechanisms. Journal of Neural Engineering 15 (1):016020. doi:10.1088/1741-2552/aa976a

1107 97. Rodriguez AR, Anderson ED, O'Neill KM, McEwan PP, Vigilante NF, Kwon M, Akum BF,
1108 Stawicki TM, Meaney DF, Firestein BL (2021) Cytosolic PSD-95 Interactor Alters Functional

1109 Organization of Neural Circuits and AMPA Receptor Signaling Independent of PSD-95 Binding.
1110 Netw Neurosci 5 (1):166-197. doi:10.1162/netn_a_00173

1111 98. De Bellis M, Pisani F, Mola MG, Rosito S, Simone L, Buccoliero C, Trojano M, Nicchia GP,
1112 Svelto M, Frigeri A (2017) Translational readthrough generates new astrocyte AQP4 isoforms
1113 that modulate supramolecular clustering, glial endfeet localization, and water transport. Glia 65
1114 (5):790-803. doi:10.1002/glia.23126

1115 99. de Bellis M, Cibelli A, Mola MG, Pisani F, Barile B, Mastrodonato M, Banitalebi S, Amiry-
1116 Moghaddam M, Abbrescia P, Frigeri A, Svelto M, Nicchia GP (2021) Orthogonal arrays of
1117 particle assembly are essential for normal aquaporin-4 expression level in the brain. Glia 69
1118 (2):473-488. doi:10.1002/glia.23909

1119 100. Simoncelli EP (1994) Design of multi-dimensional derivative filters. Proceedings -
1120 International Conference on Image Processing 1:790-794. doi:10.1109/ICIP.1994.413423

1121 101. Guizar-Sicairos M, Thurman ST, Fienup JR (2008) Efficient subpixel image registration
1122 algorithms. Opt Lett 33:156-158. doi:10.1364/ol.33.000156

1123 102. Lucas BD, Kanade T An iterative image registration technique with an application to stereo
1124 vision. In: Proceedings of the 7th International Joint Conference on Artificial Intelligence, San
1125 Francisco, CA, USA, 1981. Morgan Kaufmann Publishers Inc., pp 674-679.
1126 doi:10.5555/1623264.1623280

1127 103. Lopatin AN, Nichols CG (2001) Inward rectifiers in the heart: an update on I(K1). J Mol
1128 Cell Cardiol 33 (4):625-638. doi:10.1006/jmcc.2001.1344

1129 104. Alagem N, Dvir M, Reuveny E (2001) Mechanism of Ba(2+) block of a mouse inwardly
1130 rectifying K+ channel: differential contribution by two discrete residues. J Physiol 534 (Pt.
1131 2):381-393. doi:10.1111/j.1469-7793.2001.00381.x

1132 105. Davidson JS, Baumgarten IM (1988) Glycyrrhetinic acid derivatives: a novel class of
1133 inhibitors of gap-junctional intercellular communication. Structure-activity relationships. J
1134 Pharmacol Exp Ther 246 (3):1104-1107

1135 106. Benfenati V, Caprini M, Nicchia GP, Rossi A, Dovizio M, Cervetto C, Nobile M, Ferroni S
1136 (2009) Carbenoxolone inhibits volume-regulated anion conductance in cultured rat cortical
1137 astroglia. Channels (Austin) 3 (5):323-336. doi:10.4161/chan.3.5.9568

1138 107. Campanello L, Traver MK, Shroff H, Schaefer BC, Losert W (2021) Signaling through
1139 polymerization and degradation: Analysis and simulations of T cell activation mediated by
1140 Bcl10. PLoS Comput Biol 17 (5):e1007986. doi:10.1371/journal.pcbi.1007986

1141 108. Hirrlinger J, Hülsmann S, Kirchhoff F (2004) Astroglial processes show spontaneous
1142 motility at active synaptic terminals in situ. Eur J Neurosci 20 (8):2235-2239.
1143 doi:10.1111/j.1460-9568.2004.03689.x

1144 109. Schiweck J, Murk K, Ledderose J, Münster-Wandowski A, Ornaghi M, Vida I, Eickholt BJ
1145 (2021) Drebrin controls scar formation and astrocyte reactivity upon traumatic brain injury by
1146 regulating membrane trafficking. Nat Commun 12:1490. doi:10.1038/s41467-021-21662-x

1147 110. Faulkner JR, Herrmann JE, Woo MJ, Tansey KE, Doan NB, Sofroniew MV (2004)
1148 Reactive astrocytes protect tissue and preserve function after spinal cord injury. J Neurosci 24
1149 (9):2143-2155. doi:10.1523/JNEUROSCI.3547-03.2004

1150 111. Bardehle S, Krüger M, Buggenthin F, Schwausch J, Ninkovic J, Clevers H, Snippert HJ,
1151 Theis FJ, Meyer-Luehmann M, Bechmann I, Dimou L, Götz M (2013) Live imaging of astrocyte
1152 responses to acute injury reveals selective juxtavascular proliferation. Nat Neurosci 16 (5):580-
1153 586. doi:10.1038/nn.3371

1154 112. Sofroniew MV, Vinters HV (2010) Astrocytes: biology and pathology. Acta
1155 neuropathologica 119 (1):7-35. doi:10.1007/s00401-009-0619-8

1156 113. Curry N, Ghézali G, Kaminski Schierle GS, Rouach N, Kaminski CF (2017) Correlative
1157 STED and Atomic Force Microscopy on Live Astrocytes Reveals Plasticity of Cytoskeletal
1158 Structure and Membrane Physical Properties during Polarized Migration. Front Cell Neurosci
1159 11:104. doi:10.3389/fncel.2017.00104

1160 114. Maldonado H, Calderon C, Burgos-Bravo F, Kobler O, Zuschratter W, Ramirez O, Härtel S,
1161 Schneider P, Quest AFG, Herrera-Molina R, Leyton L (2017) Astrocyte-to-neuron
1162 communication through integrin-engaged Thy-1/CBP/Csk/Src complex triggers neurite
1163 retraction via the RhoA/ROCK pathway. Biochim Biophys Acta Mol Cell Res 1864 (2):243-254.
1164 doi:10.1016/j.bbamcr.2016.11.006

1165 115. Ferroni S, Marchini C, Nobile M, Rapisarda C (1997) Characterization of an inwardly
1166 rectifying chloride conductance expressed by cultured rat cortical astrocytes. Glia 21 (2):217-
1167 227. doi:10.1002/(sici)1098-1136(199710)21:2<217::aid-glia5>3.0.co;2-3

1168 116. Nicchia GP, Frigeri A, Liuzzi GM, Santacroce MP, Nico B, Procino G, Quondamatteo F,
1169 Herken R, Roncali L, Svelto M (2000) Aquaporin-4-containing astrocytes sustain a temperature-
1170 and mercury-insensitive swelling in vitro. Glia 31 (1):29-38. doi:10.1002/(sici)1098-
1171 1136(200007)31:1<29::aid-glia30>3.0.co;2-3

1172 117. Sloan SA, Darmanis S, Huber N, Khan TA, Birey F, Caneda C, Reimer R, Quake SR,
1173 Barres BA, Paşca SP (2017) Human astrocyte maturation captured in 3D cerebral cortical
1174 spheroids derived from pluripotent stem cells. Neuron 95 (4):779-790.e776.
1175 doi:10.1016/j.neuron.2017.07.035

1176 118. Molofsky AV, Deneen B (2015) Astrocyte development: A Guide for the Perplexed. Glia
1177 63 (8):1320-1329. doi:10.1002/glia.22836

1178 119. Molofsky AV, Krencik R, Ullian EM, Tsai H-h, Deneen B, Richardson WD, Barres BA,
1179 Rowitch DH (2012) Astrocytes and disease: a neurodevelopmental perspective. Genes Dev 26
1180 (9):891-907. doi:10.1101/gad.188326.112

1181 120. Clarke LE, Liddelow SA, Chakraborty C, Münch AE, Heiman M, Barres BA (2018)
1182 Normal aging induces A1-like astrocyte reactivity. Proc Natl Acad Sci U S A 115 (8):E1896-
1183 E1905. doi:10.1073/pnas.1800165115

1184 121. Morel L, Higashimori H, Tolman M, Yang Y (2014) VGluT1+ neuronal glutamatergic
1185 signaling regulates postnatal developmental maturation of cortical protoplasmic astroglia. J
1186 Neurosci 34 (33):10950-10962. doi:10.1523/JNEUROSCI.1167-14.2014

1187 122. Nwaobi SE, Lin E, Peramsetty SR, Olsen ML (2014) DNA methylation functions as a
1188 critical regulator of Kir4.1 expression during CNS development. Glia 62 (3):411-427.
1189 doi:10.1002/glia.22613

1190 123. Neely JD, Amiry-Moghaddam M, Ottersen O, Froehner SC, Agre P, Adams ME (2001)
1191 Syntrophin-dependent expression and localization of Aquaporin-4 water channel protein. Proc
1192 Natl Acad Sci U S A 98 (24):14108-14113. doi:10.1073/pnas.241508198

1193 124. Kuijlaars J, Oyelami T, Diels A, Rohrbacher J, Versweyveld S, Meneghello G, Tuefferd M,
1194 Verstraelen P, Detrez JR, Verschuuren M, De Vos WH, Meert T, Peeters PJ, Cik M, Nuydens R,
1195 Brône B, Verheyen A (2016) Sustained synchronized neuronal network activity in a human
1196 astrocyte co-culture system. Sci Rep 6:36529. doi:10.1038/srep36529

1197 125. Moonen G, Franck G, Schoffeniels E (1980) Glial control of neuronal excitability in
1198 mammals: I. Electrophysiological and isotopic evidence in culture. Neurochem Int 2C:299-310.
1199 doi:10.1016/0197-0186(80)90037-6

1200 126. Grisar T, Franck G, Schoffeniels E (1980) Glial control of neuronal excitability in
1201 mammals: II. Enzymatic evidence : Two molecular forms of the (Na(+),K(+))-ATPase in brain.
1202 Neurochem Int 2C:311-320. doi:10.1016/0197-0186(80)90038-8

1203 127. Perea G, Navarrete M, Araque A (2009) Tripartite synapses: astrocytes process and control
1204 synaptic information. Trends Neurosci 32 (8):421-431. doi:10.1016/j.tins.2009.05.001

1205 128. Hasel P, Dando O, Jiwaji Z, Baxter P, Todd AC, Heron S, Márkus NM, McQueen J,
1206 Hampton DW, Torvell M, Tiwari SS, McKay S, Eraso-Pichot A, Zorzano A, Masgrau R, Galea
1207 E, Chandran S, Wyllie DJA, Simpson TI, Hardingham GE (2017) Neurons and neuronal activity
1208 control gene expression in astrocytes to regulate their development and metabolism. Nat
1209 Commun 8:15132. doi:10.1038/ncomms15132

1210 129. Ghosh M, Yang Y, Rothstein JD, Robinson MB (2011) Nuclear factor-κB contributes to
1211 neuron-dependent induction of glutamate transporter-1 expression in astrocytes. J Neurosci 31
1212 (25):9159-9169. doi:10.1523/JNEUROSCI.0302-11.2011

1213 130. Pasti L, Volterra A, Pozzan T, Carmignoto G (1997) Intracellular calcium oscillations in
1214 astrocytes: a highly plastic, bidirectional form of communication between neurons and astrocytes
1215 in situ. J Neurosci 17 (20):7817-7830. doi:10.1523/JNEUROSCI.17-20-07817.1997

1216 131. Schipke CG, Kettenmann H (2004) Astrocyte responses to neuronal activity. Glia 47
1217 (3):226-232. doi:10.1002/glia.20029

1218 132. Rouach N, Glowinski J, Giaume C (2000) Activity-dependent neuronal control of gap-
1219 junctional communication in astrocytes. J Cell Biol 149 (7):1513-1526.
1220 doi:10.1083/jcb.149.7.1513

1221 133. Bernardinelli Y, Randall J, Janett E, Nikonenko I, König S, Jones EV, Flores CE, Murai
1222 KK, Bochet CG, Holtmaat A, Muller D (2014) Activity-dependent structural plasticity of
1223 perisynaptic astrocytic domains promotes excitatory synapse stability. Curr Biol 24 (15):1679-
1224 1688. doi:10.1016/j.cub.2014.06.025

1225 134. Muñoz-Lasso DC, Romá-Mateo C, Pallardó FV, Gonzalez-Cabo P (2020) Much more than
1226 a scaffold: Cytoskeletal proteins in neurological disorders. Cells 9 (2):358.
1227 doi:10.3390/cells9020358

1228 135. Tobe BTD, Crain AM, Winquist AM, Calabrese B, Makihara H, Zhao W-n, Lalonde J,
1229 Nakamura H, Konopaske G, Sidor M, Pernia CD, Yamashita N, Wada M, Inoue Y, Nakamura F,
1230 Sheridan SD, Logan RW, Brandel M, Wu D, Hunsberger J, Dorsett L, Duerr C, Basa RCB,

1231 McCarthy MJ, Udeshi ND, Mertins P, Carr SA, Rouleau GA, Mastrangelo L, Li J, Gutierrez GJ,
1232 Brill LM, Venizelos N, Chen G, Nye JS, Manji H, Price JH, McClung CA, Akiskal HS, Alda M,
1233 Chuang D-MM, Coyle JT, Liu Y, Teng YD, Ohshima T, Mikoshiba K, Sidman RL, Halpain S,
1234 Haggarty SJ, Goshima Y, Snyder EY (2017) Probing the lithium-response pathway in hiPSCs
1235 implicates the phosphoregulatory set-point for a cytoskeletal modulator in bipolar pathogenesis.
1236 Proc Natl Acad Sci U S A 114 (22):E4462–E4471. doi:10.1073/pnas.1700111114

1237

Figures and Tables

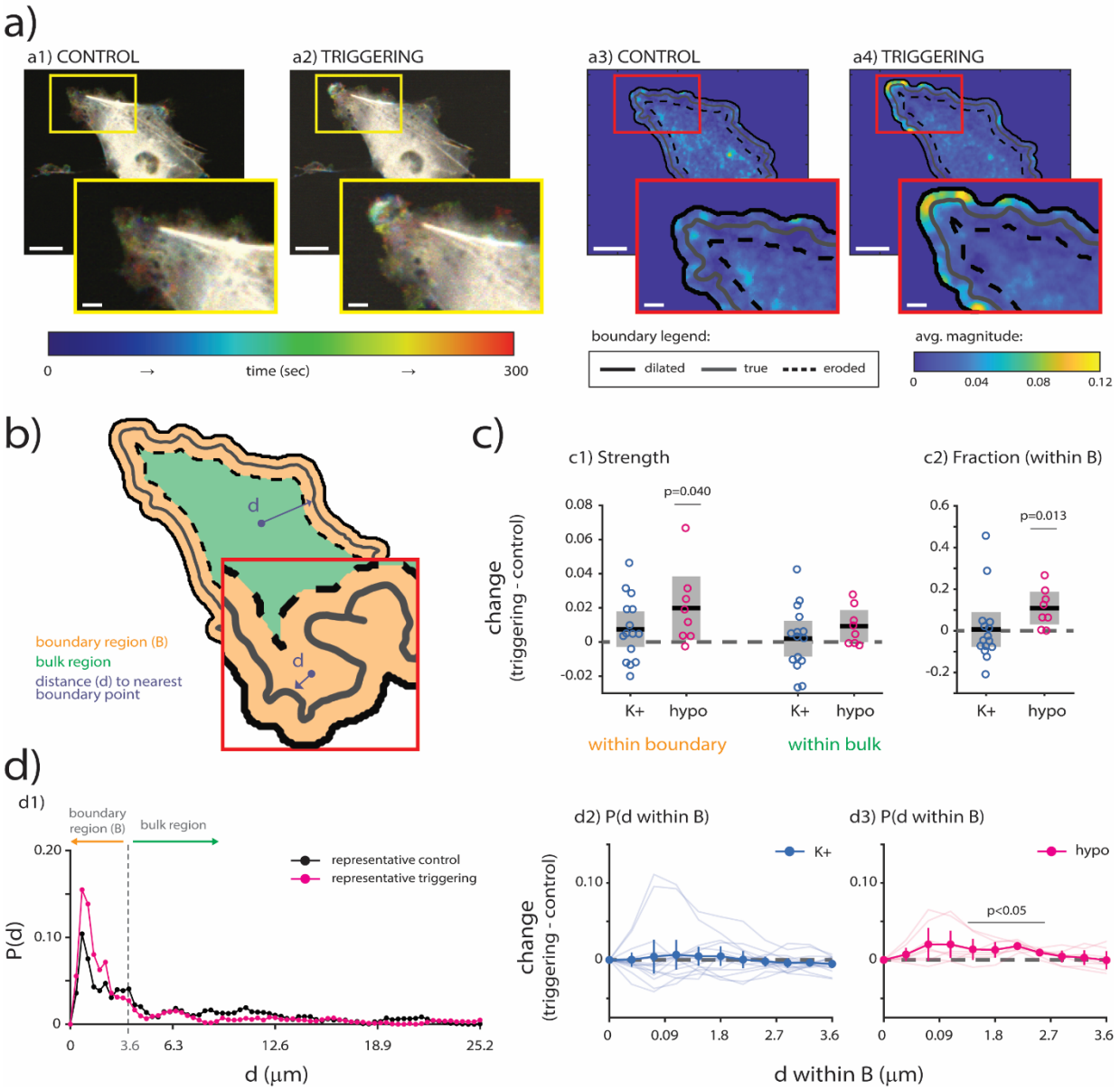

Fig. 1 Optical flow analysis reveals actin dynamics in primary astrocytes

A) Representative actin dynamics. Actin-GFP timelapse overlay for representative cell, control (A1 and inset) and triggering (A2 and inset) conditions. Colorbar indicates time. Optical flow analysis for representative cell: control (A3 and inset) and triggering (A4 and inset) conditions. Colorbar indicates average optical flow magnitude. **B)** Shape analysis [67,57,68] identifies true

1247 boundary (solid grey line). Boundary region (orange) is created by dilating (solid black line) and
1248 eroding (dashed black line) true boundary by 10 pixels and is distinct from bulk region (green).
1249 **C)** Characterizing actin dynamics. **C1)** Strength of actin dynamics within boundary (p=0.147 for
1250 control vs. K+, p=0.040 for control vs. hypo) and within bulk (p=0.696 for control vs. K+,
1251 p=0.052 for control vs. hypo). **C2)** Fraction of actin dynamics within boundary (p=0.881 for
1252 control vs. K+, p=0.013 for control vs. hypo). **D)** Distance dependence of actin dynamics.
1253 **D1)** Probability *P(d)* vs. distance from boundary *d* for representative data shown in B. **D2-**
1254 **D3)** Probability within boundary region *P(d within B)* vs. distance from true boundary within
1255 boundary region *d within B* for all cells for control vs. K+ (D2) and for control vs. hypo (D3;
1256 p=0.0499, p=0.019, p<0.001, p<0.001 at 1.44-2.52 μm). P-values determined by paired t-test (C)
1257 or by repeated measures ANOVA (D). n=15 paired cells for control vs. K+, and n=8 paired cells
1258 for control vs. hypo. Scalebars indicate 20 μm (A1-A4) or 5 μm (insets). Error bars/boxes
1259 indicate 95% confidence intervals. Solid black lines and opaque circles indicate mean.
1260 Transparent lines in D2-D3 represent individual distance curves. "Control" indicates cells
1261 imaged in standard external medium; "triggering" indicates cells imaged in isotonic high
1262 potassium solution ("K+") or hypotonic solution ("hypo").
1263

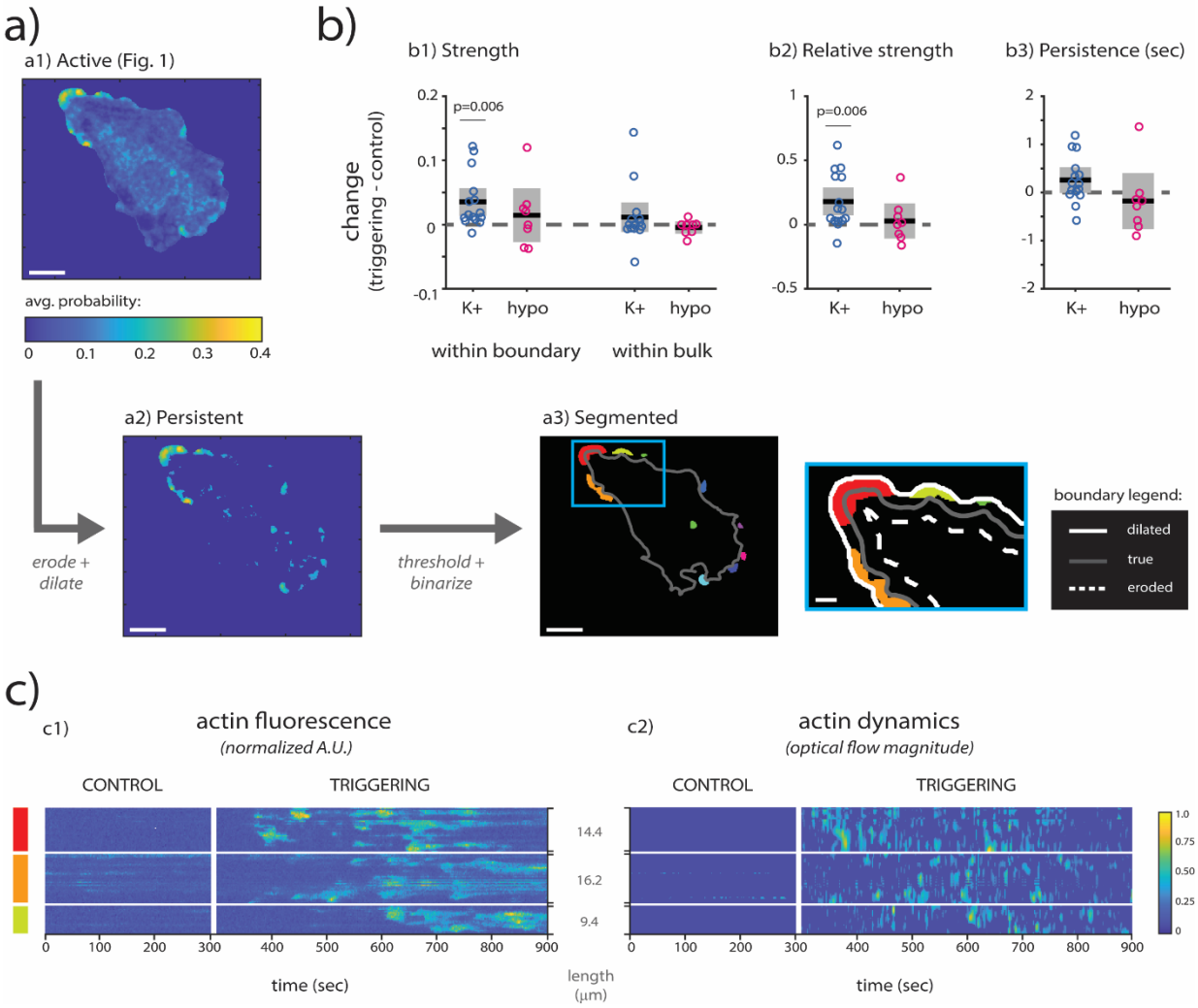

Fig. 2 Persistence analysis of actin dynamics reveal "hotspots" of actin activity

A) Identification of "hotspot" regions. Optical flow results (A1; from Fig. 1) are eroded and dilated in space and in time (A2) to identify the most persistently active regions. Regions that meet criteria are binarized and segmented (A3, inset A4) for comparison between cells and conditions. **B)** Characterization of hotspot dynamics. **B1)** Average strength of hotspot actin dynamics within boundary (p=0.006 for control vs. K+, p=0.435 for control vs. hypo) and within bulk (p=0.339 for control vs. K+, =0.298 for control vs. hypo). **B2)** Relative strength of actin dynamics (p=0.006 for control vs. K+, p=0.639 for control vs. hypo). **B3)** Average persistence of

1275 actin dynamics (p=0.056 for control vs. K+, p=0.491 for control vs. hypo). All p-values
1276 determined by paired t-test. Solid black lines indicate the mean. Grey regions indicate 95%
1277 confidence interval. **C)** Kymographs of normalized actin fluorescence (C1) and of optical flow
1278 magnitude (C2) for three largest hotspot regions from A3-A4. Grey labels between kymographs
1279 indicate lengths of regions. Colorbar indicates normalized fluorescence (C1) and optical flow
1280 magnitude (C2). n=15 paired cells for control and K+, and n=8 paired cells for control and hypo.
1281

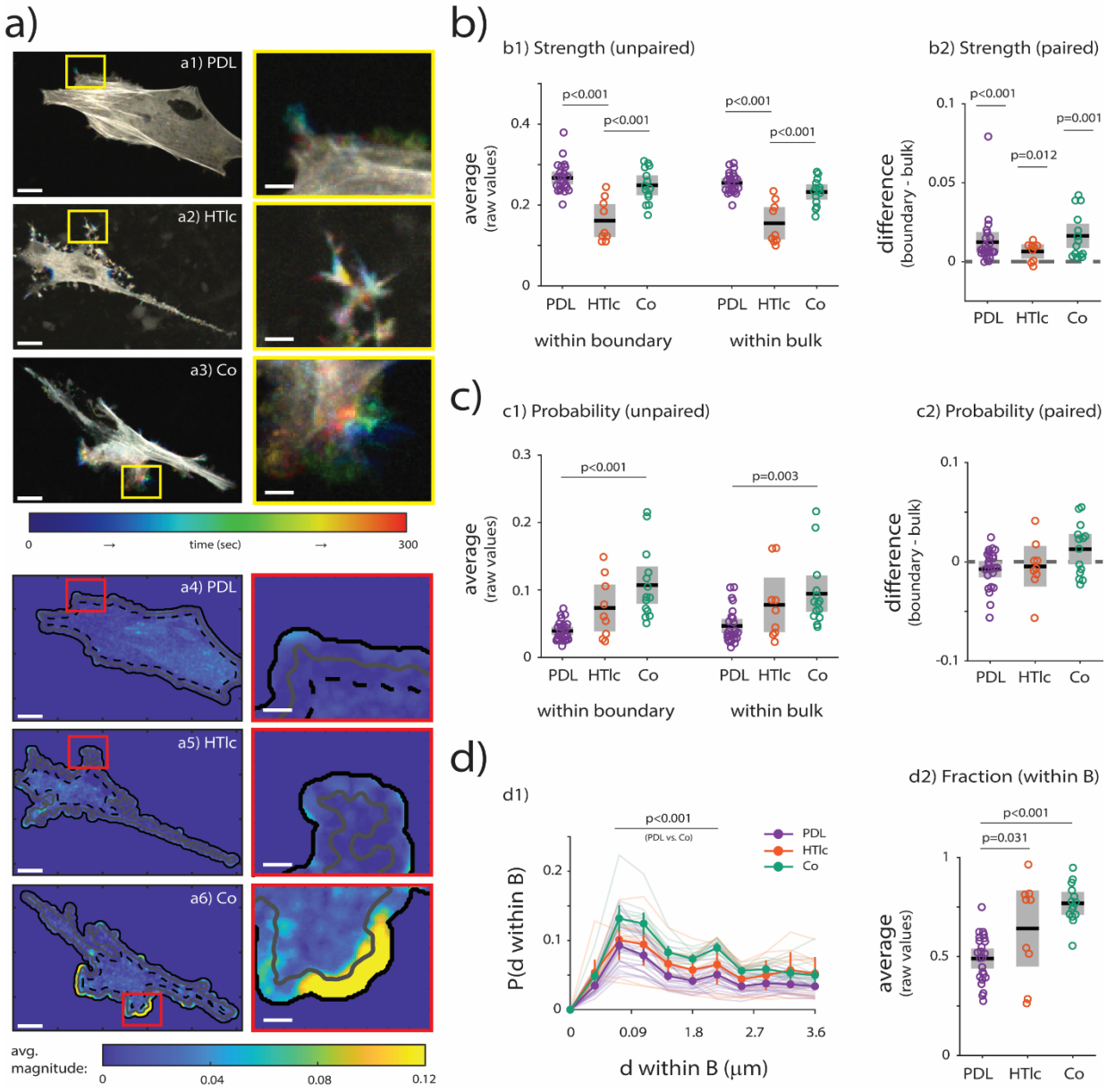

Fig. 3 Actin dynamics differs substantially in polygonal astrocytes grown on PDL compared to differentiated astrocytes grown on HTlc and to astrocytes co-cultured with neurons

A) Actin-GFP timelapse for representative cells grown on PDL-coated glass ("PDL"; A1 and inset), HTlc films ("HTlc"; A2 and inset), and co-cultured with neurons ("Co"; A3 and inset). Colorbar indicates time. Optical flow analysis for representative cells (PDL in A4 and inset;

1291 HTlc in A5 and inset; Co in A6 and inset). Colorbar indicates average optical flow magnitude.
1292 **B)** Strength of actin dynamics. **B1)** Strength of actin dynamics within boundary ($p<0.001$ for
1293 PDL vs. HTlc cells, $p<0.001$ for HTlc vs. Co cells) and within bulk ($p<0.001$ for PDL vs. HTlc
1294 cells, $p<0.001$ for HTlc vs. Co cells). **B2)** Strength of actin dynamics in boundary vs. bulk for
1295 PDL ($p<0.001$), HTlc ($p=0.011$), and Co cells ($p<0.001$). **C)** Probability of actin dynamics.
1296 **C1)** Probability of actin dynamics within boundary ($p<0.001$ PDL vs. Co cells) and within bulk
1297 ($p=0.003$ for PDL vs. Co cells). **C2)** Probability of actin dynamics in boundary vs. bulk for PDL
1298 ($p=0.072$), HTlc ($p=0.615$), and Co cells ($p=0.093$). **D)** Distance dependence of actin dynamics.
1299 **D1)** Probability within boundary region *P(d within B)* vs. distance from true boundary within
1300 boundary region *d within B* for all PDL, HTlc, and Co cells ($p<0.001$ at 0.072-2.16 μm for PDL
1301 vs. Co). **D2)** Fraction of actin dynamics within boundary ($p=0.031$ for PDL vs. HTlc, $p<0.001$
1302 for PDL vs. Co, and $p=0.122$ for HTlc vs Co). P-values determined by one-way ANOVA
1303 followed by Tukey's multiple comparisons test (B1, C1, D2), paired t-test (B2, C2), or two-way
1304 ANOVA followed by Tukey's multiple comparisons test (D1). n=24 cells for PDL, n=9 cells for
1305 HTlc, and n=14 cells for Co. Scalebars indicate 20 μm (A1-A6) or 5 μm (insets). Error
1306 bars/boxes indicate 95% confidence intervals. Solid black lines and opaque circles indicate
1307 mean. Transparent lines in D1 represent individual distance curves.
1308

1309

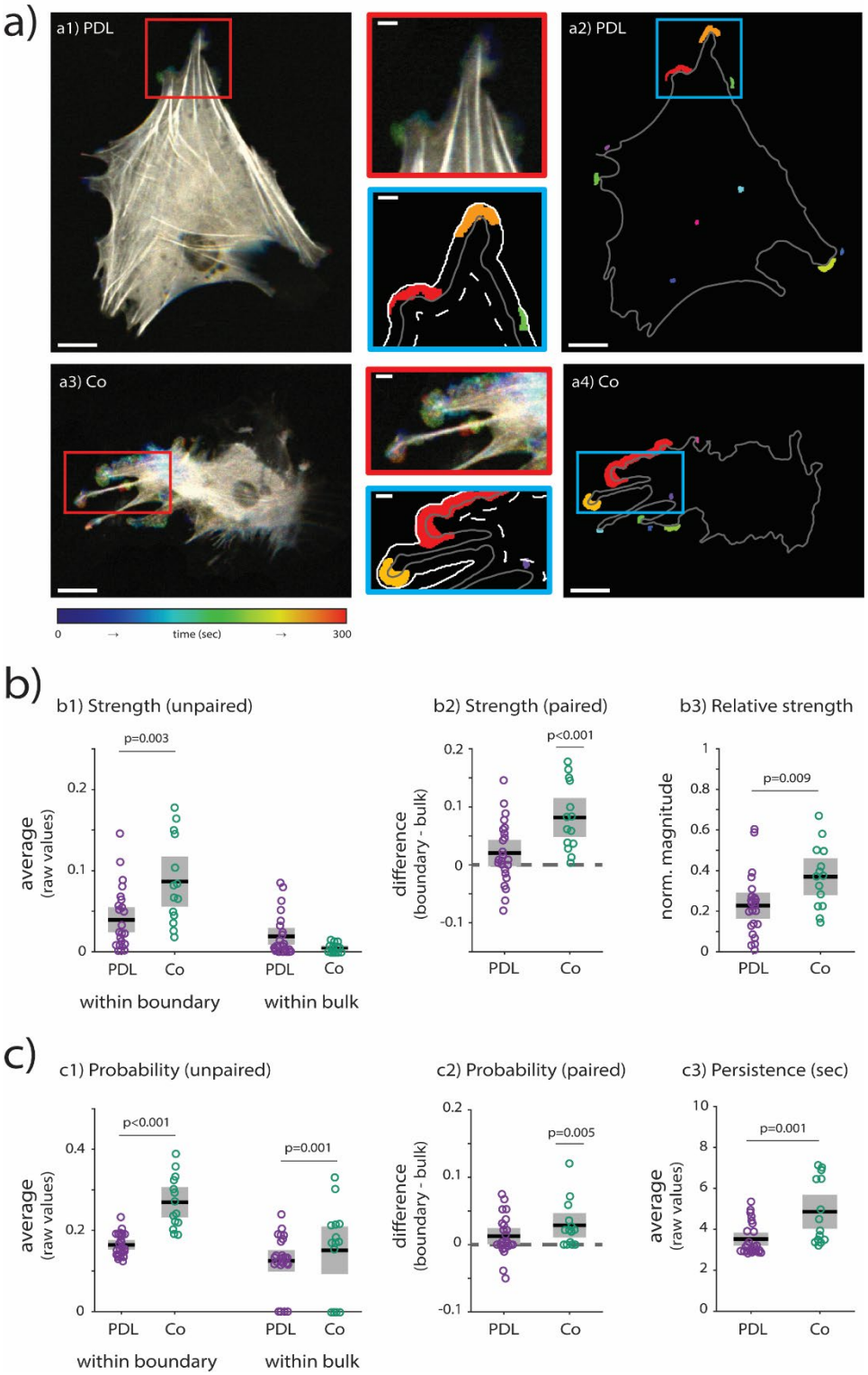

1310
1311

1312 **Fig. 4 Actin hotspot dynamics are stronger and more frequent when astrocytes are co-**

1313 **cultured with neurons**

1314 **A)** Actin-GFP timelapse for representative cells grown on PDL-coated glass ("PDL"; A1 and
1315 inset) and co-cultured with neurons ("Co"; A3 and inset). Colorbar indicates time. Persistence
1316 analysis for representative cells (PDL in A2 and inset; Co in A4 and inset). Color is used to
1317 differentiate hotspot regions. **B)** Strength of actin dynamics within hotspots. **B1)** Strength of
1318 hotspot dynamics within boundary ($p=0.003$ for PDL vs. Co cells) and within bulk ($p=0.063$ for
1319 PDL vs. Co cells). **B2)** Strength of hotspot dynamics in boundary vs. bulk for PDL ($p= 0.075$)
1320 and Co cells ($p<0.001$). **B3)** Relative strength of hotspot dynamics for PDL vs. Co ($p=0.009$).
1321 **C)** Probability of actin dynamics within hotspots. **C1)** Probability of hotspot dynamics within
1322 boundary ($p<0.001$ for PDL vs. Co cells) and within bulk ($p=0.001$ for PDL vs. Co cells).
1323 **C2)** Strength of actin dynamics in boundary vs. bulk for PDL ($p=0.051$) and Co cells ($p=0.005$).
1324 **C3)** Persistence of actin dynamics for PDL vs. Co ($p=0.001$). P-values determined by two-
1325 sample t-test (B1, B3, C1, C3) or paired t-test (B2, C2). n=24 cells for PDL, and n=14 cells for
1326 Co. Scalebars indicate 20 μm (A1-A4) or 5 μm (insets). Error bars/boxes indicate 95%
1327 confidence intervals. Solid black lines and opaque circles indicate mean.
1328

1329

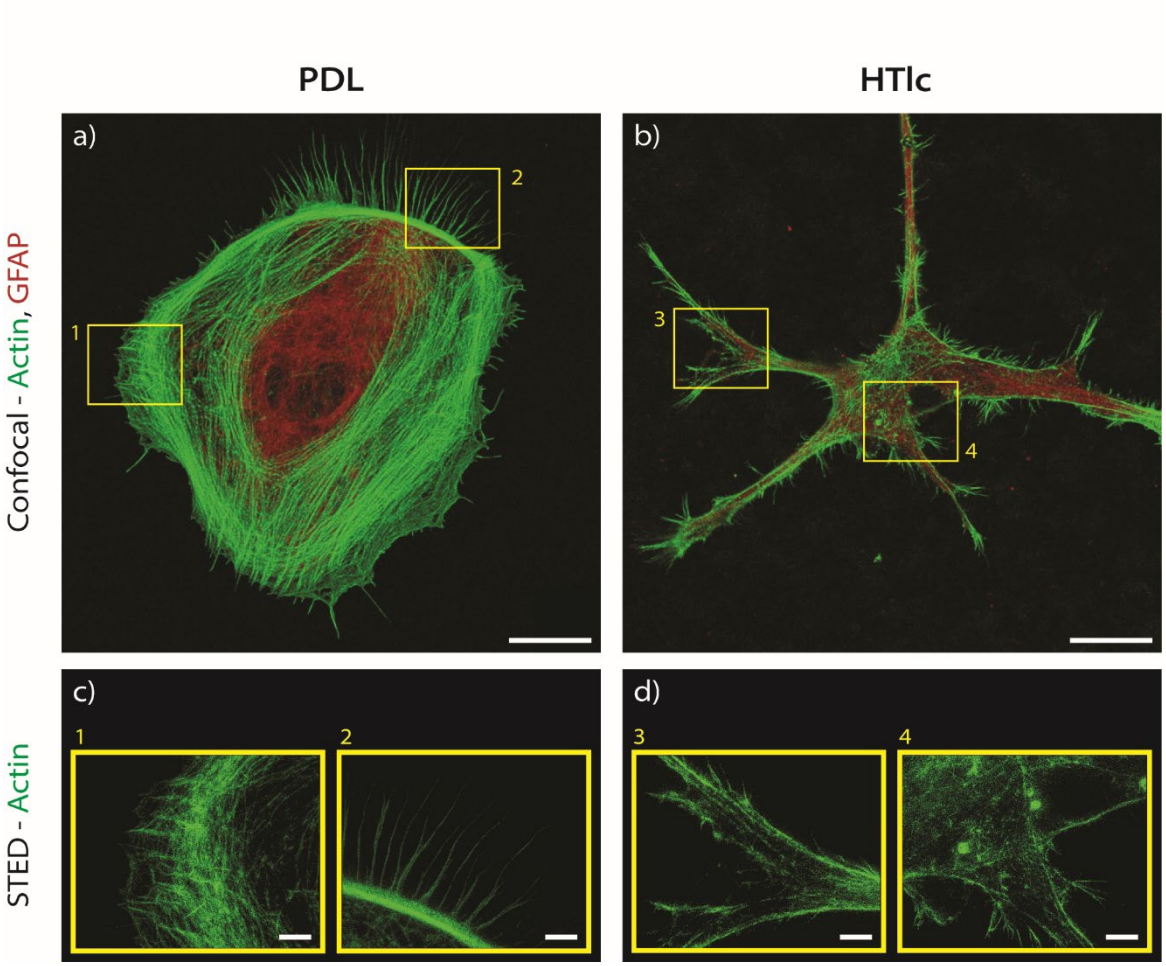

1330
1331
1332 **Fig. 5 STED microscopy visualizes nanoscale actin structure within primary astrocytes**
1333 **grown on PDL and on HTlc**

1334 **A-B)** Confocal microscopy images of representative astrocytes grown on PDL-coated glass (A)
1335 or on HTlc films (B) for five days, fixed, and stained for actin (green) and GFAP (red). Scalebars
1336 indicate 10 µm. **C-D)** Superresolution images taken via STED microscopy of cells grown on
1337 PDL (C) and on HTlc (D) of boxed yellow regions from A and B. Scalebars indicate 2.5 µm.

1338

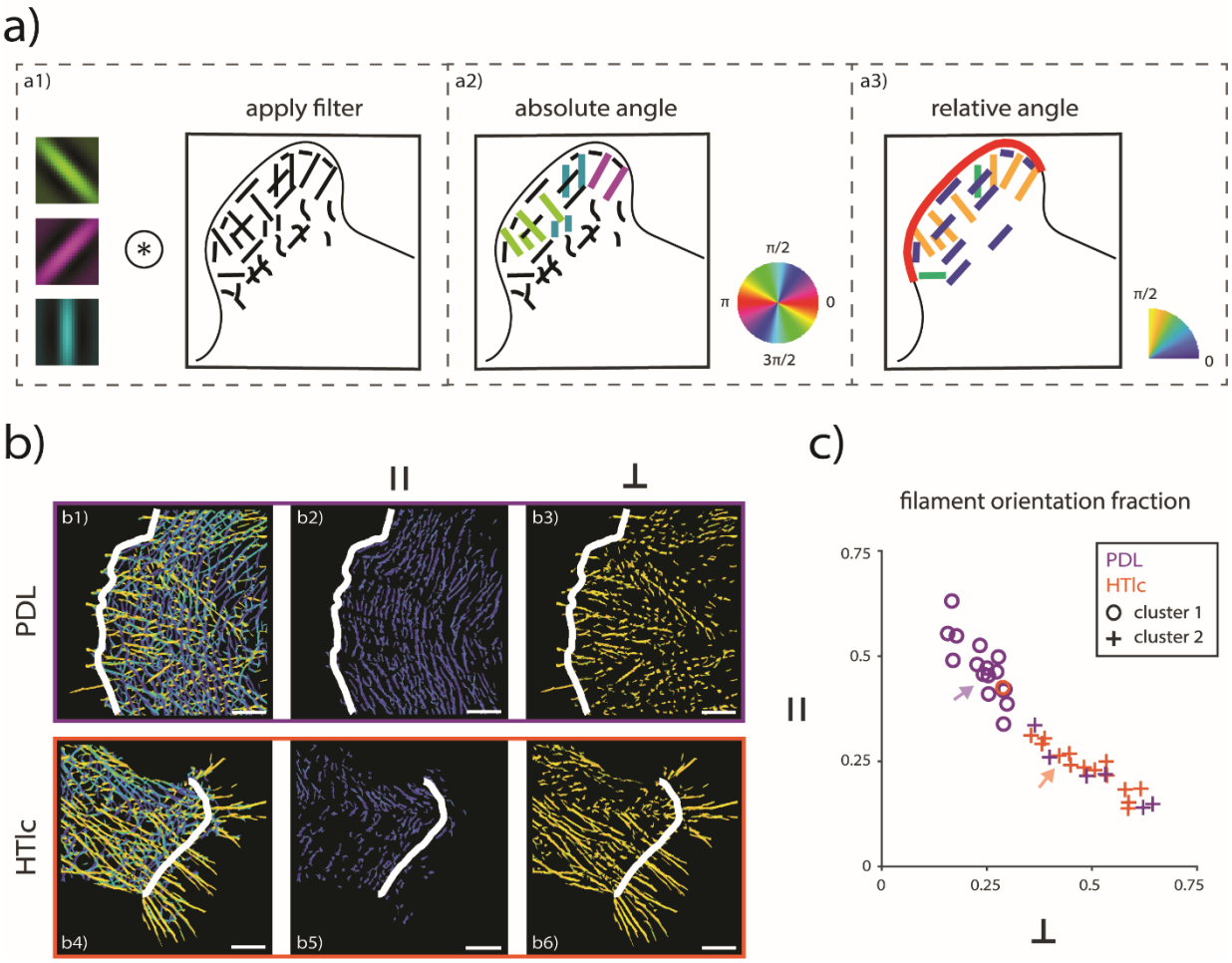

Fig. 6 Filtering STED images with a rotating, anisotropic LoG kernel reveals differences in nanoscale actin structure for astrocytes grown on PDL versus on HTlc

A) Extraction of relative angle information from actin filaments. **A1)** STED images are convolved with a rotating, anisotropic LoG kernel. **A2)** Filtering extracts actin bundles and a best match angle that is relative to the MATLAB frame ("absolute angle") with a range of [0, 2π] (shown as full colorwheel). **A3)** A leading edge boundary (red) is drawn manually and is used to transform actin angles to be relative to the closes boundary point ("relative angle") with a range of [0, π/2] (shown as a quarter colorwheel). **B)** Output from A for representative cells (PDL in B1-B3, HTlc in B4-B6). All relative angles, parallel angles only (range of [0, π/6]), and

1351 perpendicular angles only (range of [π/3, π/2]) for representative PDL (B1, B2, B3, respectively)
1352 and HTlc (B4, B5, B6, respectively) cells. Solid white lines indicate leading edge boundary.
1353 Scalebars indicate 2.5 μm. **C)** Parallel (y-axis) vs. perpendicular (x-axis) fractions of actin
1354 detected within PDL (purple) and HTlc (orange) astrocytes. A hierarchical cluster analysis
1355 reveals two distinct clusters (cluster 1: open circles, cluster 2: crosses). Arrows indicate
1356 representative cells. n=22 cells for PDL, and n=15 cells for HTlc.
1357

1358

	Parameter	Actin	GFAP
Confocal	WLL (488 nm) intensity, %	10	10
	Gain	25	25
STED	WLL (488 nm) intensity, %	40	
	STED (592 nm) intensity, %	97	
	Gain	200	

1359

1360 **Table 1: Imaging parameters.** Parameters used for STED and confocal imaging of fixed

1361 astrocytes on PDL and HTlc.

1362